



The South Purulia Shear Zone, eastern India: Its anatomy and implication for timing the Rodinia-age collision in the eastern part of the Central Indian Tectonic Zone

Anwesa Banerjee¹, Nicole Sequeira², Nathan Cogné³, Prabhakar Naraga¹, and Abhijit Bhattacharya⁴

¹Department of Earth Sciences, Indian Institute of Technology Bombay, Powai, Mumbai 400076, India

²School of Earth, Ocean and Atmospheric Sciences, Goa University, Taleigao Plateau, Goa 403206, India

³Géosciences Rennes, UMR 6118, CNRS, Université de Rennes, Rennes 35000, France

⁴180B Hijli Co-Operative Society, Kharagpur 721306, India

ABSTRACT

The Proterozoic Central Indian Tectonic Zone (CITZ) is an ~1500-km-long collision zone between the North India and the South India blocks. The age of collision is debated, but constraining the age of collision is crucial for reconstructing the paleogeographic position of India in the Precambrian. In this study, mesoscale structures, metamorphic pressure-temperature path, U-Pb zircon dates, and monazite chemical dates are combined to constrain the collision age. In the eastern part of the CITZ, the North Singhbhum Mobile Belt (NSMB) comprising 1.5–1.3 Ga low-grade phyllites and schists and the 1.88 Ga Ranibandh granitoid are juxtaposed with the Chottanagpur Gneiss Complex (CGC; eastern CITZ) dominated by 1.76 Ga anatectic basement gneisses intruded by 1.67 Ga, 1.57 Ga, and pre-collisional 1.02 Ga felsic intrusives. The juxtaposition of the disparately evolved crustal domains along the South Purulia Shear Zone (SPSZ) involved top-to-the-south thrusting consistent with amphibolite facies loading. Continued oblique N-S shortening of the thickened crust led to nucleation of ESE-striking, steeply dipping left-lateral transpressional shear zones tens of kilometers wide that obliterated pre-collisional structures in the rheologically weak NSMB phyllites and schists but are weakly developed in the rheologically strong CGC rocks. The 1.02–0.91 Ga oblique collision between the North India and South India blocks along the SPSZ suggests the paleopole data pre-dating the collision are unlikely to ascertain the paleogeographic position of the Indian landmass because the landmass did not exist in its entirety before 1.02–0.91 Ga. But the paleopole data may help locate the North India and South India blocks independent of each other.

1. INTRODUCTION

Little unanimity exists among researchers regarding the reconstructed paleogeographic positions of the Great Indian landmass retrieved from

Nicole Sequeira <https://orcid.org/0000-0002-9970-7553>

Proterozoic paleopole data (Li et al., 2008; Pisarevsky et al., 2013; Merdith et al., 2021). In some Rodinia supercontinent reconstructions, India is positioned at the periphery of Rodinia (Rivers, 2015; Bhattacharya et al., 2023; Fig. 1A); others suggest that India at ca. 1.0 Ga was located close to the pole (Spencer et al., 2013) or close to the equator (Merdith et al., 2021).

Research in the last decade shows that the Precambrian crust of the Indian landmass assembled by aggregation of crustal domains along regional scale shear zones, e.g., the Shillong-Meghalaya Gneiss Complex, NE India (Chatterjee et al., 2007); the Phulad Shear Zone, NW India (Chatterjee et al., 2020); the Central Indian Tectonic Zone (CITZ), north-central India (Chattopadhyay et al., 2020; Banerjee et al., 2021; Bhattacharya et al., 2023); the Achankovil Shear Zone, South India (Paharaj et al., 2021); the Mahakoshal Belt, central India (Deshmukh et al., 2021); and the Eastern Ghats Belt, SE India (Biswal et al., 2007; Nasipuri et al., 2018). Precise determination of the timing of deformation, metamorphic, and magmatic events demonstrates that these shear zones are terrane-boundary shear zones formed as a result of welding of crustal domains (Chatterjee et al., 2007, 2020; Rekha et al., 2011; Paharaj et al., 2021). This implies that the Indian landmass was not a coherently evolved Precambrian crust but instead is a mosaic of crustal domains with diverse evolutionary histories and welded between the late Paleoproterozoic and the early Paleozoic.

The E-striking CITZ (Fig. 1A) is an ~1500-km-long, highly tectonized zone composed of Proterozoic crystalline rocks (Yedekar et al., 1990; Acharyya and Roy, 2000; Acharyya, 2001; Bhowmik et al., 2012; Bhattacharya et al., 2023; Mohanty, 2023) with rare Archean inheritance (Mohanty, 2023). The CITZ is wedged between the South India block and the North India block (Fig. 1B). However, the lithological-structural and petrological-chronological characteristics of the CITZ and the adjacent blocks are poorly delineated except by a few studies in the Chottanagpur Gneiss Complex (CGC) (Bhattacharya et al., 2019; Sequeira and Bhattacharya, 2021) (Fig. 1C) and in the Godhra–Chhota Udepur sector (Banerjee et al., 2022a, 2022b, 2022c) in the western CITZ (Fig. 1B). Also, in the west-central parts of the CITZ (Fig. 1B), the margins of the North India block–South India block–CITZ are obscured by the Cretaceous Deccan basalts and recent riverine sediments. Due to this lack of adequate coverage of lithological-structural and

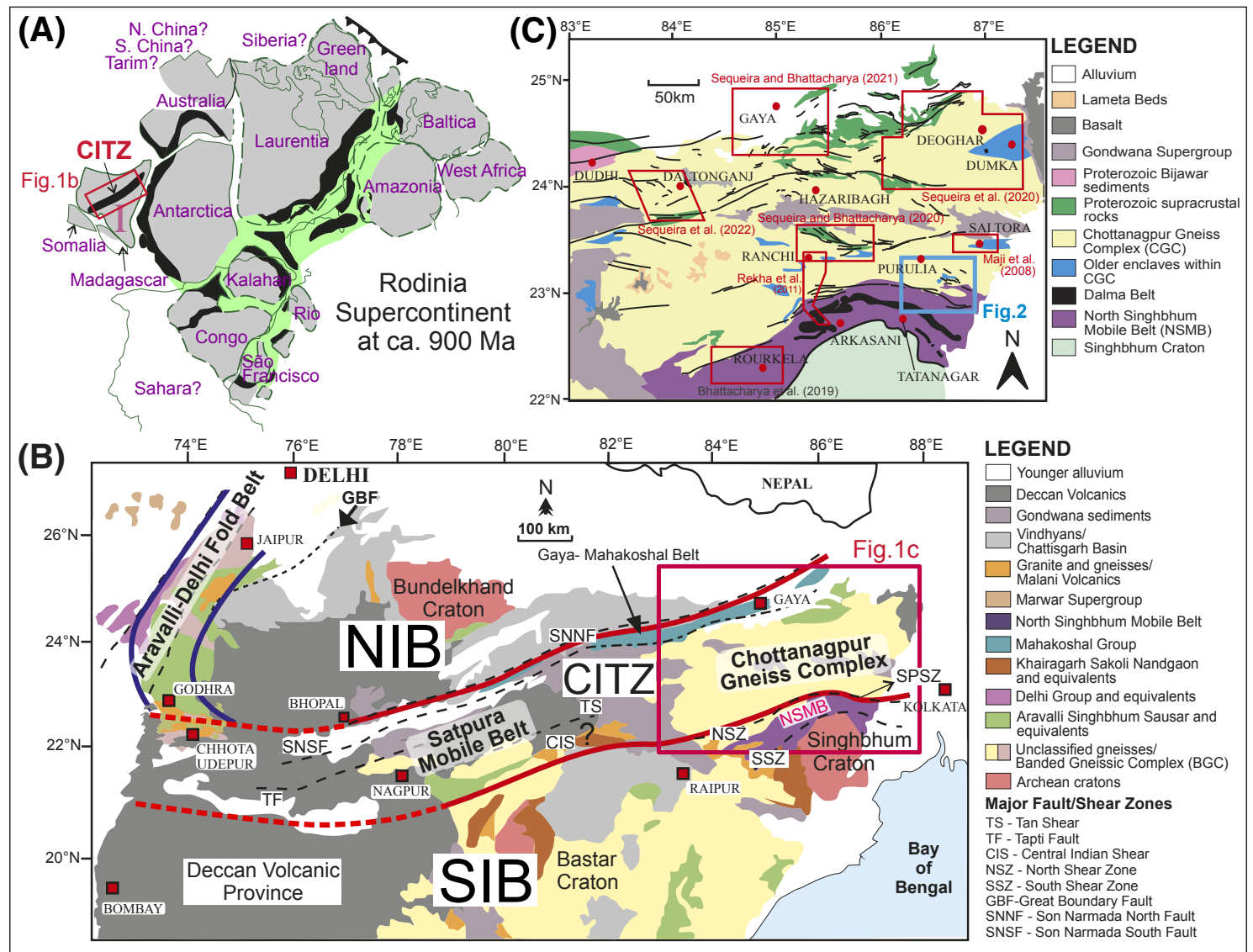


Figure 1. (A) Rodinia reconstruction showing location of Central Indian Tectonic Zone (CITZ) as part of the circum-global 1.1–0.9 Ga collision belt (Bhattacharya et al., 2023). Black thick lines are Rodinia-age collision zones. CITZ is shown in box. (B) Generalized geological map of Central India (adopted from Banerjee et al., 2021) showing CITZ demarcated by red lines between North India block (NIB) and South India block (SIB). Red box shows Chottanagpur Gneiss Complex (CGC). (C) Generalized geological map of CGC with red boxes showing areas previously studied (Maji et al., 2008; Rekha et al., 2011; Bhattacharya et al., 2019; Sequeira and Bhattacharya, 2020, 2021; Sequeira et al., 2020, 2022). Blue box shows location of area examined in this study (Figs. 2 and 3) across contact between CGC and North Singhbhum Mobile Belt (NSMB). In the box in (B), South Purulia Shear Zone (SPSZ) (existing models) is demarcated by black line separating CGC and NSMB.

petrological-geochronological data in the E-striking crustal domains within and adjacent to the CITZ, the demarcation of the South India block (and North India block) from the CITZ is blurred. Thus, either all rocks with E-striking fabrics may be deemed to be part of the CITZ or the CITZ may comprise differently evolved crustal blocks and some blocks along the margins may belong to the South India block–North India block. This study is designed to address this issue.

Mohanty (2023) suggested the North India block–South India block collision occurred in the early Paleoproterozoic (2100–2000 Ma). On the other hand, Chakrabarty et al. (2023) suggested the northern margin of the CITZ is a late Paleoproterozoic–early Mesoproterozoic (1700–1600 Ma) collision zone that welded the North India block with the CITZ. By contrast, Bhattacharya et al. (2023) proposed the CITZ forms a part of the circum-global Rodinia-aged (1030–900 Ma) collision zone along which the North India and South India blocks collided (Fig. 1B). Neither Chakrabarty et al. (2023) nor Mohanty (2023) ascertained whether the CITZ evolved as a coherently evolved single block or is composed of differently evolved crustal domains that welded sequentially or contemporaneously. To address these shortcomings, we examine the South Purulia Shear Zone (SPSZ) along the southern margin of the CGC (Figs. 1B and 1C), located at the eastern extremity of the CITZ. More specifically, we determine the tectonic significance of the SPSZ at the southern margin of the CITZ (Fig. 1C) based on an analysis of mesoscale structures, pressure-temperature (*P-T*) path reconstruction, and U–Pb zircon and U–Th–total Pb monazite chronology across the SPSZ.

2. GEOLOGICAL BACKGROUND

The E-striking SPSZ (Acharyya et al., 2006; Dwivedi et al., 2011; Acharjee et al., 2016) is an ensemble of highly tectonized rocks (Figs. 1B, 1C, 2A, and 2B). The intensely mylonitized lithologies in the SPSZ comprise deformed and metamorphosed felsic volcanics, epiclastic meta-greywackes, meta-argillites, quartzites, and mafic-ultramafic schists (Acharyya et al., 2006). The shear zone is straddled by the crustal domains of the CGC in the north and the North Singhbhum Mobile Belt (NSMB) in the south (Figs. 1B, 1C, and 2B), the latter of which fringes the Paleoproterozoic to Neoproterozoic Singhbhum Craton (Fig. 1C) (Prabhakar and Bhattacharya, 2013; Chaudhuri et al., 2018; Olierook et al., 2019).

The CGC (Figs. 1B and 1C) is composed of 1.68–1.50 Ga anatectic basement quartzofeldspathic and garnet–sillimanite–K-feldspar–bearing metapelitic gneisses and foliated charnockites intruded by 1.45–1.35 Ga granitoids and 1.02–0.95 Ga granitoids (Rekha et al., 2011; Bhattacharya et al., 2019; Mukherjee et al., 2018a, 2018b; Sequeira and Bhattacharya, 2020, 2021; Sequeira et al., 2020, 2022). Also reported from the CGC are linear belts of greenschist–amphibolite facies schists, meta-dolomites, and mafic schists (Sequeira and Bhattacharya, 2020) and deformed anorthosite massifs (Chatterjee et al., 2008) and carbonatites (Basu and Bhattacharyya, 2014). The early Neoproterozoic granitoids in the CGC are proposed to be broadly coeval with the oblique N–S collision between the North India and South India blocks (Banerjee et al., 2021; Sequeira et al., 2020, 2022).

By contrast, the NSMB is divided by the Dalma Belt (Figs. 1C, 2A, and 2B) into two parts, e.g., the northern NSMB (N-NSMB) and the southern NSMB (S-NSMB) (Rekha et al., 2011). The Dalma Belt itself is dominated by meta-igneous rocks of mafic and ultramafic compositions. The N-NSMB (Figs. 1B and 1C) is composed of multiply deformed greenschist facies transitional to amphibolite facies phyllites and schists (muscovite–chlorite–biotite–quartz dominated) and micaceous (muscovite) quartzites interleaved with mafic schists (chlorite–actinolite–plagioclase) and minor proportions of meta-carbonates (calcite–tremolite–plagioclase–clinozoisite–quartz) (Mahato et al., 2008; Maji et al., 2008; Rekha et al., 2011). Several lens-shaped bodies of deformed granitoid plutons occur in the N-NSMB, e.g., the Kulilpal granite (Ghosh, 1959a, 1959b), the Barabazar granite (Dwivedi et al., 2011), and the Ranibandh granite. For the A-type Kulilpal granite with within-plate chemical character, Sastry et al. (2013) determined a whole-rock Rb–Sr isochron age of 1792 ± 98 Ma and a Pb–Pb isochron age of 1863 ± 80 Ma. For the A-type Barabazar granitoid, Dwivedi et al. (2011) obtained whole-rock isochron Pb–Pb and Rb–Sr ages of 1771 ± 210 Ma (emplacement) and 971 ± 58 Ma (isotopic re-homogenization). In published geological maps (Acharyya et al., 2006; Dwivedi et al., 2011; Acharjee et al., 2016), the steep-dipping SPSZ is depicted by a line (Fig. 2A) coinciding with the southern margin of the CGC. The N-NSMB adjacent to the CGC is characterized by 1.0–0.9 Ga mid-crustal prograde metamorphism (Mahato et al., 2008).

The S-NSMB is characterized by 1.5–1.3 Ga amphibolite facies clockwise metamorphism related to the collision along the Singhbhum Shear Zone (Fig. 2B) with the Singhbhum Craton (Mahato et al., 2008). Johnson et al. (1993), however, obtained a Pb–Pb age of 1766 ± 82 Ma for uraninite and sulfide mineralization in the Singhbhum Shear Zone; Rao et al. (1979) obtained uraninite Pb–Pb ages of 1580–1480 Ma for the shear zone. By comparison, the emplacement ages of granitoids in the S-NSMB are older than the likely age of formation of the Singhbhum Shear Zone. For example, Bhattacharya et al. (2015) obtained a sensitive high-resolution ion microprobe (SHRIMP) U–Pb zircon date of 1861 ± 6 Ma for the Arkasani granophyre in the S-NSMB close to the Singhbhum Shear Zone. Bhattacharya et al. (2015, p. 497) obtained a younger SHRIMP U–Pb zircon igneous crystallization date of 1631 ± 6 Ma from an “unfoliated felsic volcanic rock” from the base of the Dalma volcanic suite. For the Dalma suite of meta-igneous rocks, comparable whole-rock ages have been determined by a host of authors, e.g., 1619 ± 38 Ma (Rb–Sr; Roy et al., 2002), 1677 ± 11 Ma (Rb–Sr, Pb–Pb; Sarkar et al., 1986), and 1638 ± 38 Ma (Rb–Sr; Sengupta et al., 1994).

3. MESOSCALE STRUCTURES ACROSS THE SOUTH PURULIA SHEAR ZONE

Based on the observation of 275 outcrops and traverses linking these outcrops, an area extending across the SPSZ was structurally mapped (Fig. 3A). The area is divided into (1) a southern NSMB domain comprising quartz–muscovite phyllites and schists interleaved with mafic schists and deformed granitoids and (2) a northern CGC domain comprising anatectic gneisses, granitoids, and bands of garnet ± staurolite muscovite–biotite schists. The southern domain is

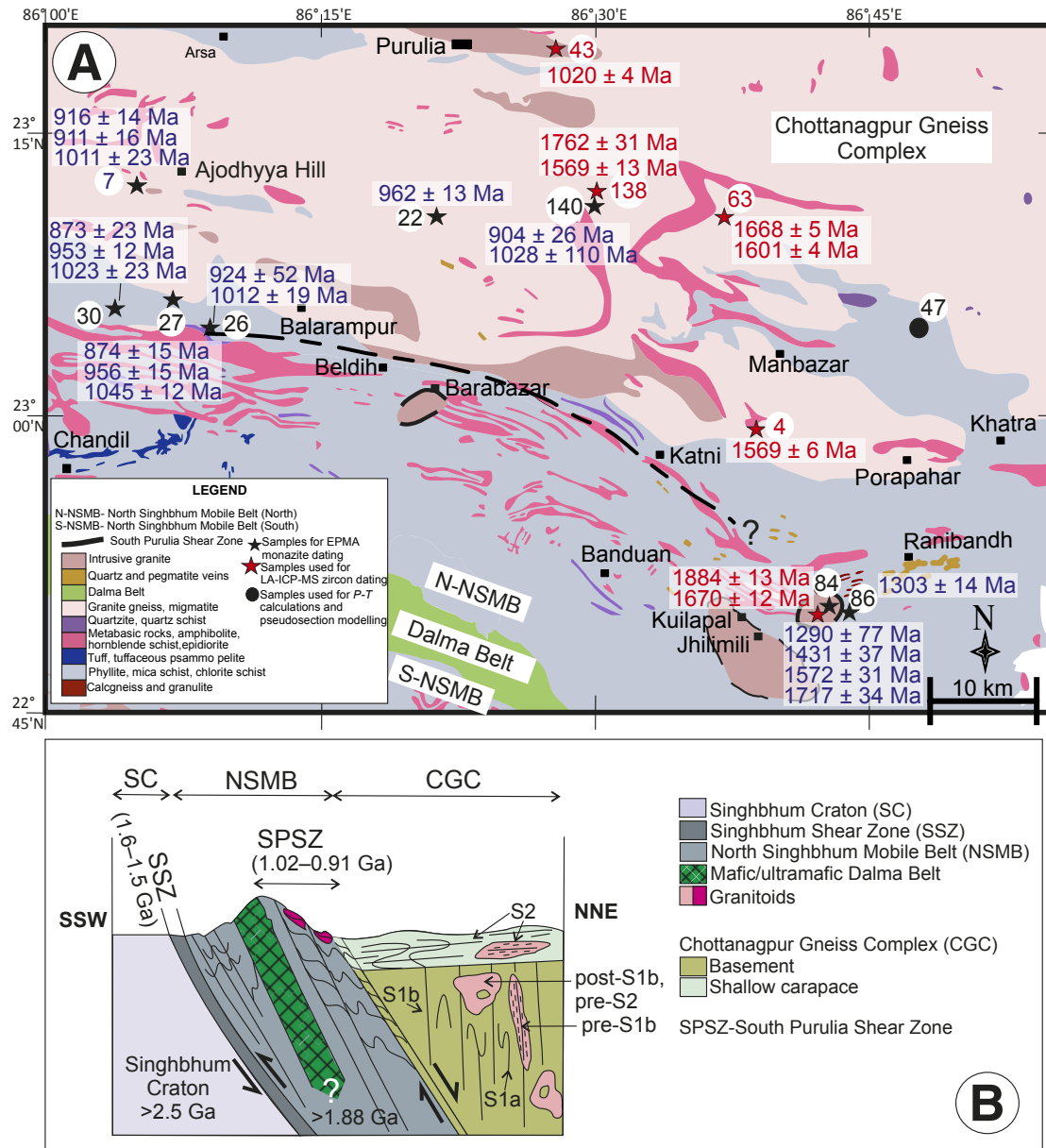


Figure 2. (A) Simplified lithological map of area investigated (modified after Geological Survey of India (2006), Puruliya (2001a), and Bankura (2001b)). Locations of samples used for U-Pb zircon geochronology (solid red stars) and monazite geochronology (solid black stars) and pressure-temperature (P-T) pseudosection modeling (solid black circle) alongside sample number. Sample numbers within white circles have “WN.” as prefix, except sample 7 neighboring Ajodhya Hill in NW corner of map, which has “YD.” as prefix. U-Pb zircon dates and Th-U-total Pb monazite dates obtained in this study are shown (data source, Table 2; see text). EPMA—electron probe micro-analysis; LA-ICP-MS—laser ablation inductively coupled plasma mass spectrometry. (B) Schematic section transverse across North Singhbhum Mobile Belt (NSMB) and Chottanagpur Gneiss Complex (CGC) showing essential features of the NSMB crustal domain wedged between Singhbhum Craton (in the south) and CGC (in the north). Thin black lines indicate traces of different foliations present in the rocks. See text for detailed discussion. For clarity of presentation, subscripts used in main text to designate different generations of planar and linear structures and deformations are shown in normal font size.

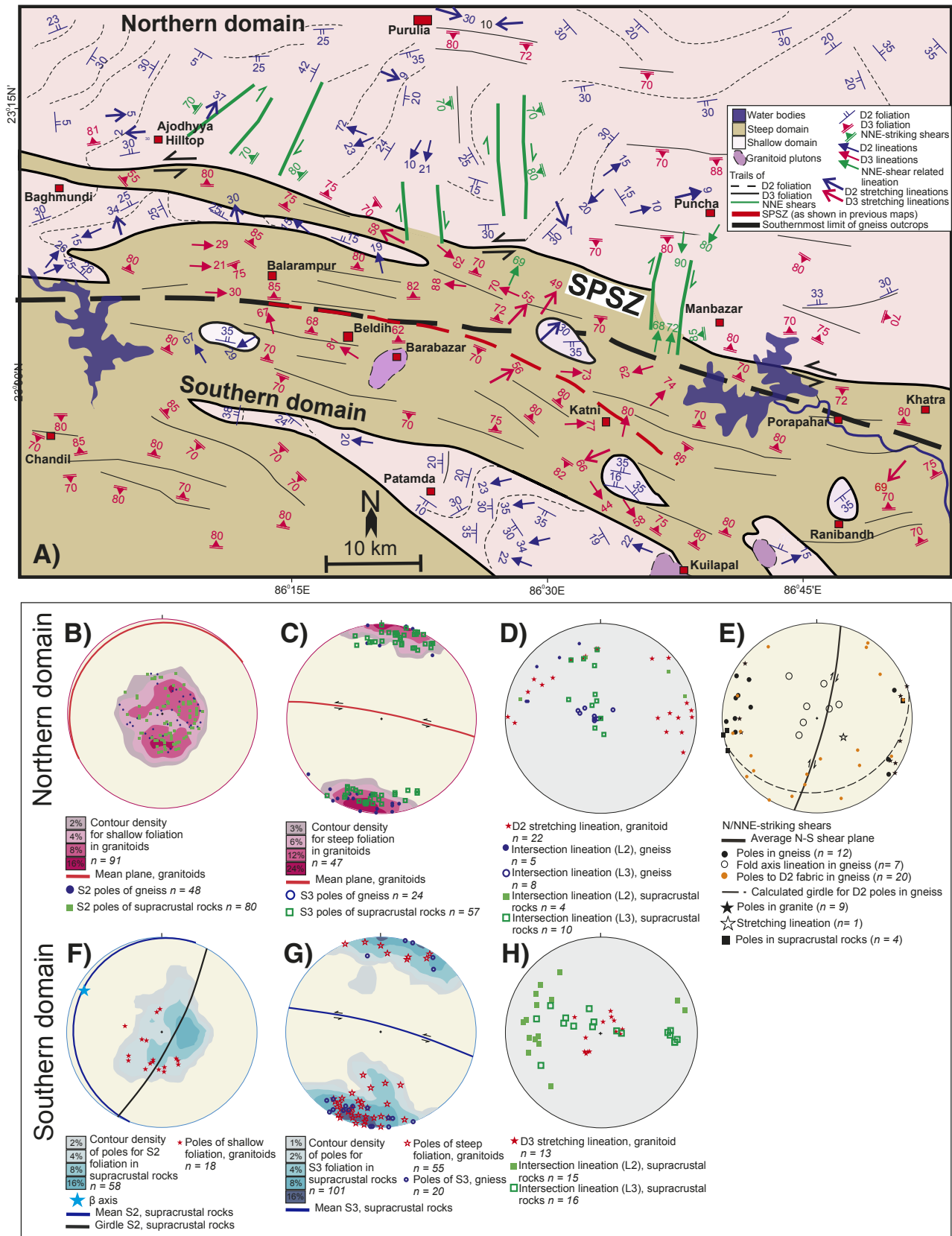


Figure 3. (A) Structural map of study area (the aerial extent is the same as in Fig. 2) showing planar and linear structures in two structural domains (see text for discussion). Dashed black line marks southern limit of Chottanagpur Gneiss Complex anatectic gneisses of northern domain; dashed red line is trace of South Purulia Shear Zone (SPSZ) proposed by earlier workers (see text). (B–H) Stereographic projections of planar and linear structures for northern domain (B–E) and southern domain (F–H). S₂ and S₃ refer to planar structures corresponding to D₂ and D₃ deformations, respectively (details in text). D₂ and D₃ stretching lineations are also shown. For clarity in presenting details in the figure, normal-sized fonts instead of subscripts are used for designating generations of structural elements.

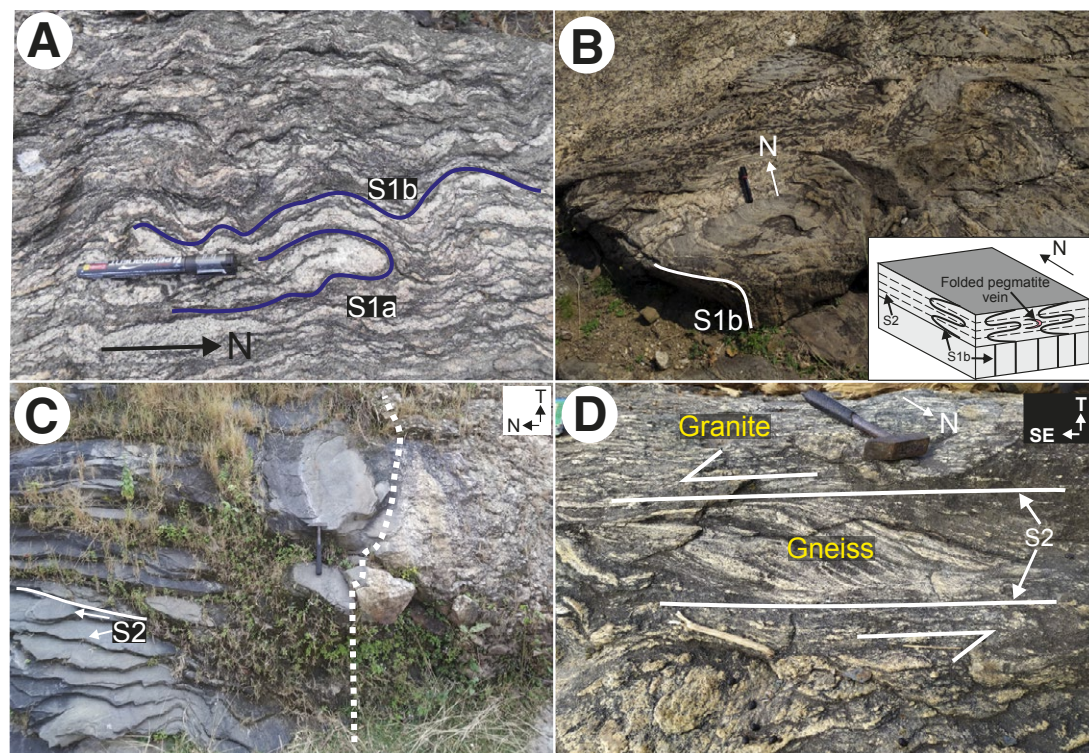
characterized by steeply dipping (dip >70°) ESE-striking tectonic foliations and steeply inclined folds. The ESE-striking folds with steeply dipping axial planes weaken northwards and at best are discontinuous and locally developed in the northern domain. The northern domain is dominated by shallowly dipping (dip <35°) structures such as gently dipping mylonitic foliation in mylonitic granitoids and recumbent to gently inclined folds in anatectic gneisses traversed by discontinuous ESE- and NNE-striking shear zones (Fig. 3A).

3.1 Northern Domain

In the anatectic basement gneisses, the earliest planar structures comprise alternate leucocratic and mesocratic layers designated S_{1a} (D_{1a} deformation) separated by selvages of ferromagnesian minerals (biotite modally dominant

relative to hornblende) (Fig. 4A). The S_{1a} layering occurs as rare rootless hinges of isoclinal folds in the intrafolial domains of a pervasive S_{1b} mineral segregation layering (Fig. 4A). The limbs of the folded S_{1a} leucocratic layers sub-parallel to S_{1b} fabric commonly exhibit pinch-and-swell structures (Fig. 4A); this implies that the pre- to syn- D_{1a} leucosomes solidified prior to D_{1b} deformation. Also, the lack of leucosome pods at D_{1b} boudin necks and the absence of leucosomes along axial planes of D_{1b} folds indicate melt productivity in the anatectic gneisses decreased from D_{1a} to D_{1b} fabric-forming events. In the gneisses, quartz, plagioclase, K-feldspar, biotite (modally abundant relative to hornblende), and ilmenite are the dominant minerals, in decreasing order of abundance; titanite, apatite, monazite, and zircon occur as accessory minerals. Garnet is rare. In a few outcrops, the N- to NNE-striking steeply dipping S_{1b} layering in the gneisses is modified by tight to isoclinal recumbent to gently inclined folds; however, axial planar fabric (S_2) associated with D_2 folds is

Figure 4. Field photographs of planar and linear structures in northern domain. Top (T) is indicated in section views and North (N) is shown in all images. Pen measures 15 cm in length. (A) North-striking steeply dipping S_{1b} gneissic layering in anatectic gneiss showing D_{1b} intrafolial folds on S_{1a} leucosome layers and biotite-defined foliation in melanosome. (B) D_2 recumbent folds and associated S_2 axial planes (background) structurally overlying N-striking steeply dipping S_{1b} gneissic layers in anatectic quartzofeldspathic gneisses (foreground). Inset sketch depicts structural relations. The same pen used in the other images is the object used for scale in the photo. (C) Shallowly dipping (S_2) quartzofeldspathic gneiss intruded by weakly foliated coarse-grained granitoid (lithological contact shown by broken line). (D) Lens-shaped enclave of anatectic gneiss (banded, in center) within shallowly dipping (S_2) granitoid mylonite (drawn-out K-feldspar porphyries) indicates apparent top-to-the-south sense of shear. Note post- D_{1b} , pre- D_2 granite lacks S_{1b} mineralogical layering in the gneiss enclave. (E) Shallowly dipping (S_2) granitoid mylonite (L-S tectonite) exhibiting westerly plunging stretching lineations defined by elongate K-feldspar clasts. Inset sketch shows the structural relations in the photograph. (F) Shallowly dipping (S_2) anatectic gneiss intruded by granitoid deformed by S_3 shear zones. Sketch depicting structural relations is shown as inset. (G) K-feldspar clasts (arrow) in E-striking granitoid mylonite exhibiting apparent north-down shear sense in section parallel to steeply plunging stretching lineation and perpendicular to foliation. (H) E-striking melt-bearing shear zones (S_3) with apparent sinistral sense of movement truncating former shallowly dipping S_2 fabrics in anatectic gneisses. (I) En echelon extensional shear zones (trace shown by continuous line) with north-directed displacement in micaceous quartzite. Half arrow heads demarcate displacement by brittle deformation of quartzite band along extensional shear zones (opposing arrows). For clarity in presenting details in the figure, normal-sized fonts instead of subscripts are used for designating generations of structural elements.



weakly developed (Fig. 4B). Compared to the steeply dipping S_{1b} layering, the D_2 folds are exposed at shallower crustal depth (Fig. 4B), identical with the structures shown in the Hundru Falls region (Sequeira and Bhattacharya, 2020) further to the NW within the CGC and in the south of Gaya (Sequeira and Bhattacharya, 2021) along the northern margin of the CGC.

A few pre- S_{1b} granitoids lack the S_{1a} fabric in the gneisses, but most granitoids are post-tectonic with respect to S_{1b} (Figs. 4C and 4D). The post- S_{1b} granitoids are S and/or S-L tectonites, exhibiting sub-horizontal to gently inclined tectonic foliations (Figs. 4C–4F). The poles of the S_2 foliation in the granitoids overlap with those of the S_2 axial planes in the gneisses (Fig. 3B). An apparent top-to-the-south movement on S_2 is observed in the sigmoid gneiss enclave within the shallowly dipping foliated granite (Fig. 4D). The stretching lineations on the shallowly dipping S_2 foliations in the granitoids are defined by K-feldspar augen and quartz lentils (Fig. 4E). These D_2 stretching lineations in granitoids are somewhat scattered, but the majority of lineations plunge gently to the WNW or ESE (Fig. 3D). The plunges of the D_2 fold hinges in the gneisses and in the sparse muscovite-biotite schists within the northern domain exhibit a wide scatter on a gently inclined plane, but a majority of them are non-coaxial with the D_2 stretching lineations (Fig. 3D).

The shallowly inclined (Fig. 3B) S_2 axial planes in the gneisses (Fig. 4B) and the S_2 fabric in the mylonite granitoids (Figs. 4C and 4D) are dissected by ESE-striking, steeply dipping south-vergent D_3 shear zones (Figs. 3C and 4F–4H). These D_3 shear zones exhibit apparent north-down (Fig. 4G) and apparent left-lateral shear senses (Fig. 4H). In the northernmost parts of the northern domain, the D_3 shear zones host felsic leucosomes (Fig. 4H). Neighboring the leucosomes in the D_3 shear zones, the folds are tighter than those distal from the melt-bearing zones (Fig. 4H). This indicates a close temporal-spatial association between the D_3 strain accumulation and melt localization (cf. Vigneresse and Burg, 2000). In other words, some of the granitoids (Fig. 4H) in the CGC interior were locally melt bearing during D_3 deformation.

Distal from the E- to ESE-striking D_3 shear zones, the shallowly dipping structures in the gneisses and the granitoids exhibit upright to steeply inclined gentle folds, the hinges of these folds plunging toward ESE or WNW at outcrop scale (Fig. 3D). Figure 4I depicts brittle-ductile shear zones showing apparent north-down sense movement indicating an extensional deformation event post-dating D_2 deformation. This structural feature, however, is observed in a single outcrop, and therefore the spatial extent of this deformation event is uncertain.

Besides the E- to ESE-striking D_3 shear zones, the northern domain is traversed by several N- to NNE-striking ductile shear zones (Figs. 5A and 5B) and associated folds (Fig. 5C) at outcrop scale as well as at the regional scale (Fig. 3A). The N- to NNE-striking shear zones demonstrably post-date the S_2 fabric, but the contemporaneity of these shear zones with respect to the ESE-striking S_3 shear zone fabric could not be ascertained at the outcrop scale. At the outcrop scale, the N- to NNE-striking shear zones are antithetic to the E- to ESE-striking D_3 shear zones; the two sets of shear zones are tentatively considered to be contemporaneous. The N- to NNE-striking shear zones in the granitoids (Fig. 5A) and in the gneisses (Figs. 5B and 5C) are steeply dipping

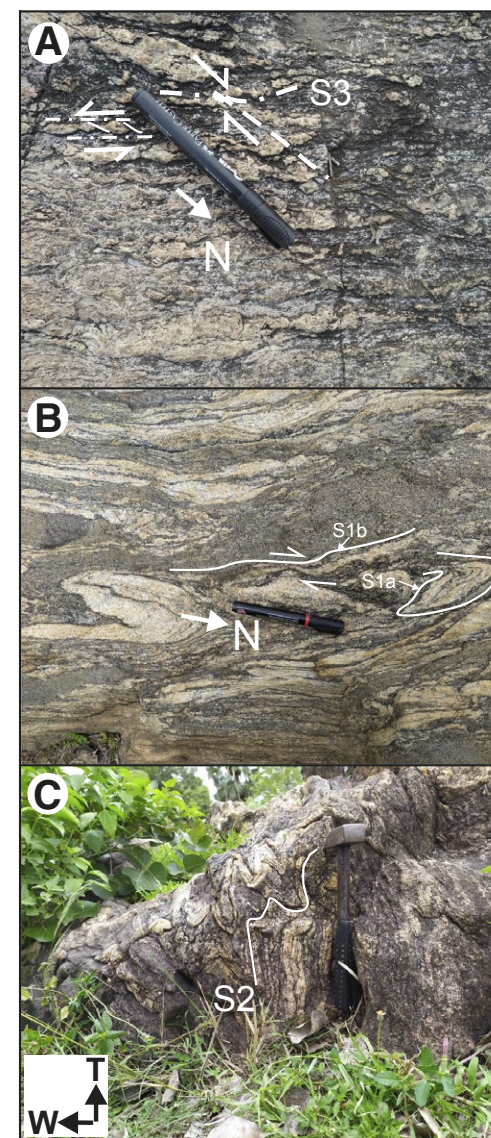


Figure 5. Field photographs of planar and linear structures in N- to NNE-striking shear zones (northern domain). (A) N-striking dextral shear zones antithetic to ENE-striking mylonite fabric with sinistral kinematics in granitoids. (B) Type III interference patterns on anatectic layers (S_{1b}) in quartzofeldspathic gneiss hosted within N-striking dextral shear zones. (C) Moderately to steeply plunging tight folds in anatectic gneisses hosted within the N- to NNE-striking shear zone. T—top. For clarity in presenting details in the figure, normal-sized fonts instead of subscripts are used for designating generations of structural elements.

(Fig. 3E) and exhibit a dextral sense of movement (Fig. 5A); stretching lineations are rare. The folds associated with the steeply dipping N- to NNE-striking shear zones in the gneisses exhibit thickened hinges and attenuated limbs. The folds vary from upright to steeply inclined, and the hinge lines of the open to tight folds are moderately to steeply plunging (Fig. 3E). These N- to NNE-striking shear zones are uncommon in the southern domain.

3.2 Southern Domain

The mesoscale structures in the southern domain (Fig. 3) are shown in Figure 6, and the spatial variation in D_2 and D_3 fold structures is schematically depicted in Figure 7. In the southernmost part of the domain (Figs. 2 and 3A), the ensemble of finely laminated quartz schist and phyllite (Figs. 6A and 6B), ferruginous quartzites (Fig. 6C), and mafic schists exhibit a pervasive ESE-striking steeply dipping tectonic fabric, S_3 (Fig. 3G). In these southernmost parts of the SPSZ, the pre- S_3 fabrics are either completely transposed and obliterated (Fig. 6A) or preserved as curved foliation traces (Fig. 6B) and as relic folds in the intrafolial domains of the steeply dipping fabric (Fig. 6C). The E- to ESE-striking penetrative steeply dipping mylonite fabric is associated with steeply plunging stretching lineations (Figs. 3H and 6A), and the hinges of the D_3 reclined to steeply plunging folds are broadly collinear (Figs. 3H and 7). Porphyroblast-matrix relations and S-C fabrics indicate a sinistral shear sense (Figs. 6D and 6E) and a persistent north-down (Fig. 6B) sense of movement in the lithodemic units, viewed in X-Z section (Fig. 7). Northwards within the SPSZ and in the northern CGC domain, the sense of movement (Figs. 4G and 4H) and the orientations of the steeply dipping S_3 fabric (Figs. 4C, 4D, 4G, and 4H) are identical albeit sparsely developed.

In the northern parts of the SPSZ, several shallowly dipping structural domains are identified within the steeply dipping southern domain (Figs. 3A and 3F). These shallowly dipping domains are dominated by recumbent to gently inclined folds on a former schistosity (Fig. 6F). These folds are correlated with the D_2 deformation in the northern domain. In these shallowly dipping domains, the east and west closing folds associated with the D_3 deformation are open to tight, possess steeply inclined axial planes, and exhibit moderate to gently plunging non-cylindrical hinge lines (Figs. 3H, 6G, and 6H). We infer the shallowly dipping sectors in the steeply dipping southern domain (Fig. 3A) are zones of low D_3 strain where the former fabrics and fold structures are preserved. In the D_3 low-strain, shallowly dipping domains, the plunges of D_3 fold axes are sub-horizontal to gentle (Figs. 3A and 3H). Both the shallowly dipping and steeply dipping fabrics are preserved in the Kulalpal granite body (Ghosh, 1959a, 1959b).

3.3 Synthesis

Following the arguments proposed by Dewey et al. (1998) and Fossen and Tikoff (1998), we suggest the steeply dipping SPSZ characterized by steeply

plunging stretching lineations is a left-lateral transpressional shear zone (Fig. 7). The ESE-striking shear zone is tens of kilometers wide and extends as far south as the meta-igneous rocks of the Dalma Belt (Fig. 3A). Thus, designating the SPSZ by a single line (Acharyya et al., 2006; Dwivedi et al., 2011; Acharjee et al., 2016) is an oversimplification. In the west-central part of the area, the trace of the SPSZ invoked by the earlier authors coincides with the southernmost limit of the CGC anatectic gneisses and granitoids (Fig. 3A; this study). But in the east-central part of the SPSZ, the two lines diverge; i.e., the southernmost limit of the lithodemic units of the CGC (Fig. 3A) deviates from the trace of the SPSZ proposed by the earlier authors.

The shear zone (Fig. 3A) comprises lithodemic units of the northern domain (CGC) as well as the N-NSMB rocks to the south. We demonstrate that both the northern and the southern domains experienced recumbent to gently inclined folding and nucleation of shallowly dipping mylonite fabrics induced by apparent top-to-the-south thrusting (D_2 deformation; Figs. 4D and 7). Subsequently, the thrust-related structures were overprinted by E- to ESE-striking transpressional shear zones (D_3 deformation) with sinistral (Figs. 4H, 6D, and 6E) and dominantly north-down sense of movement (Fig. 4G). Both the D_2 and D_3 structures were produced by crustal shortening.

Within the SPSZ, the intensity of S_3 fabric development and the geometry and orientations of the D_3 folds are variable (Fig. 7). In the southernmost parts of the SPSZ, the S_3 fabrics are pervasively developed, and the hinges of reclined to steeply plunging D_3 folds on S_2 fabrics occurring as relicts in the S_3 intrafolial domains are sub-parallel to the steeply plunging stretching lineations (Fig. 7). This S_3 fabric weakens northwards within the SPSZ, where open to tight non-cylindrical D_3 folds with gently plunging to moderately plunging D_2 folds on the pre- S_2 fabrics become dominant (Fig. 7). The weakening of the D_3 strain northwards within the SPSZ and in the CGC is possibly due to the rheological differences between the northern domain (dominated by quartzofeldspathic gneisses and deformed granitoids) and southern domain (dominated by phyllites and mica- and/or chlorite-actinolite schists). The dominance of rheologically weak phyllosilicate minerals in the lithodemic units in the southern parts of the SPSZ led to partitioning of the bulk strain into strike-slip-dominated simple shear deformation (Fig. 7). This resulted in the near-obliteration of pre- D_2 fabrics and structures in the southern domain (Figs. 6A and 6B) except in a few outcrops (Fig. 6C). But the preservation of pre- D_3 structures in the rheologically more competent northern parts of the SPSZ and in the CGC domain was in all likelihood caused by the weakening of bulk strain and promoted by the dip-slip (north-down) movement along S_3 planes (Fig. 7; cf. Ghosh et al., 2003).

The D_3 deformation in the southern domain occurred at greenschist facies transitional to amphibolite facies (450–500 °C) manifested by the widespread muscovite + biotite ± chlorite assemblage in mica schists and phyllites (Fig. 8A) and amphibole + chlorite + plagioclase ± epidote assemblages in mafic schists (Fig. 8B). Dynamic recrystallization in core-mantled structured feldspar clasts (Fig. 8C) in post- D_2 granitoids indicate the D_3 deformation occurred at similar temperature. However, in the northernmost part of the CGC domain, quartz

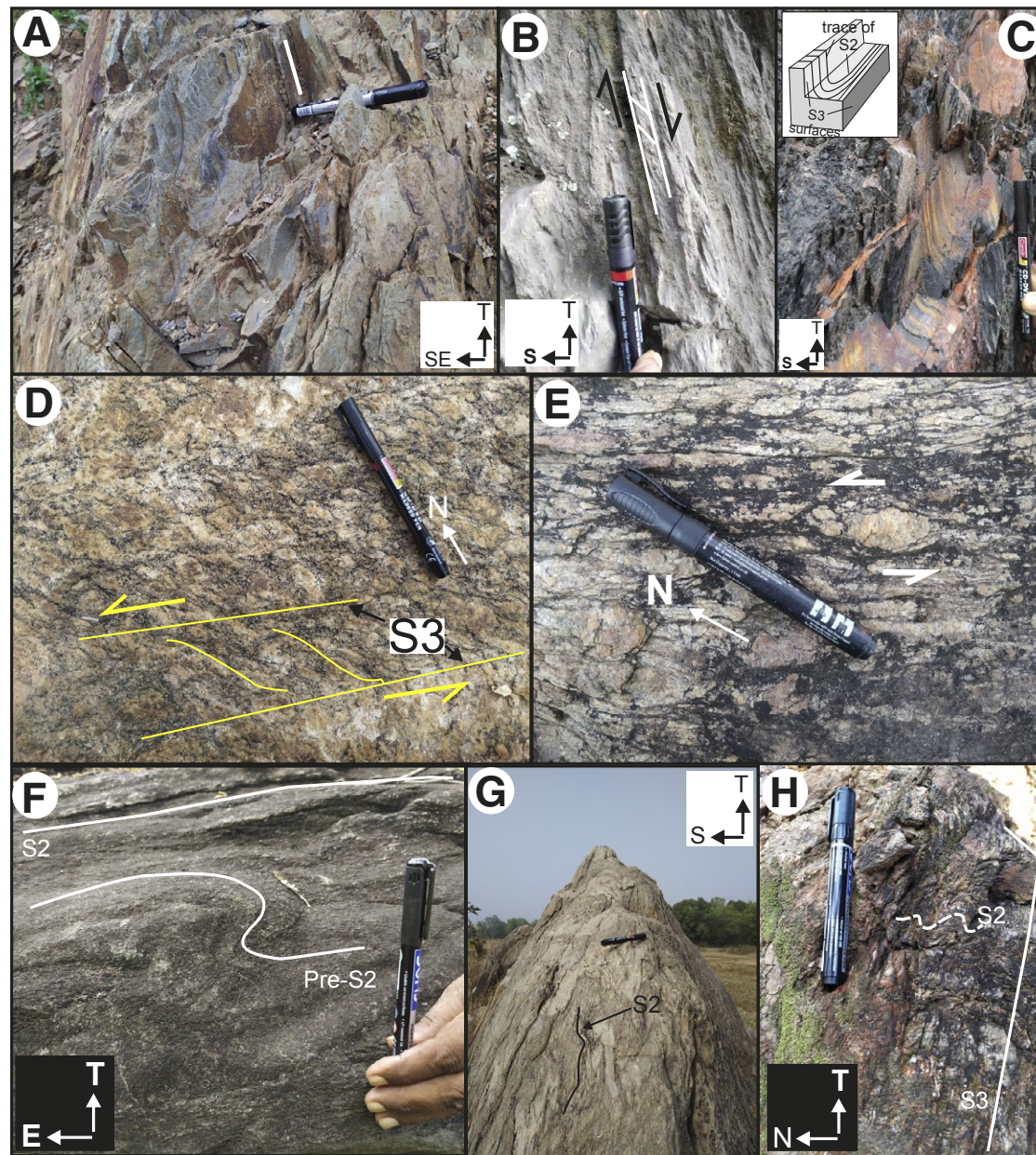


Figure 6. Field photographs of planar and linear structures in southern domain. T—top direction in section views. (A–C) Steeply dipping nature of the shear zone fabric (S_3) in quartz phyllites (A, B) and banded quartzite (C). (A) Down-dip intersection lineation (white line) defined by trace of a folded surface on steeply dipping S_3 shear zone fabric. (B) S-C fabric on X-Z surface showing apparent north-down sense of movement on D_3 shear zone fabric in phyllites. (C) Steeply plunging D_3 reclined folds on S_2 mineral segregation layering in intrafolial domains of S_3 in banded ferruginous quartzites. (D, E) S-C fabrics in Ranibandh granitoid showing sinistral shear sense associated with D_3 deformation. (F) Profile section of intrafolial recumbent D_2 folds in muscovite-biotite schists on pre- S_2 fabric in D_3 low-strain domains. (G, H) Moderately plunging hinges of D_3 folds on D_2 mineral segregation layering in micaeous quartzites. Note the E-W-striking S_3 axial planes. For clarity in presenting details in the figure, normalized fonts instead of subscripts are used for designating generations of structural elements.

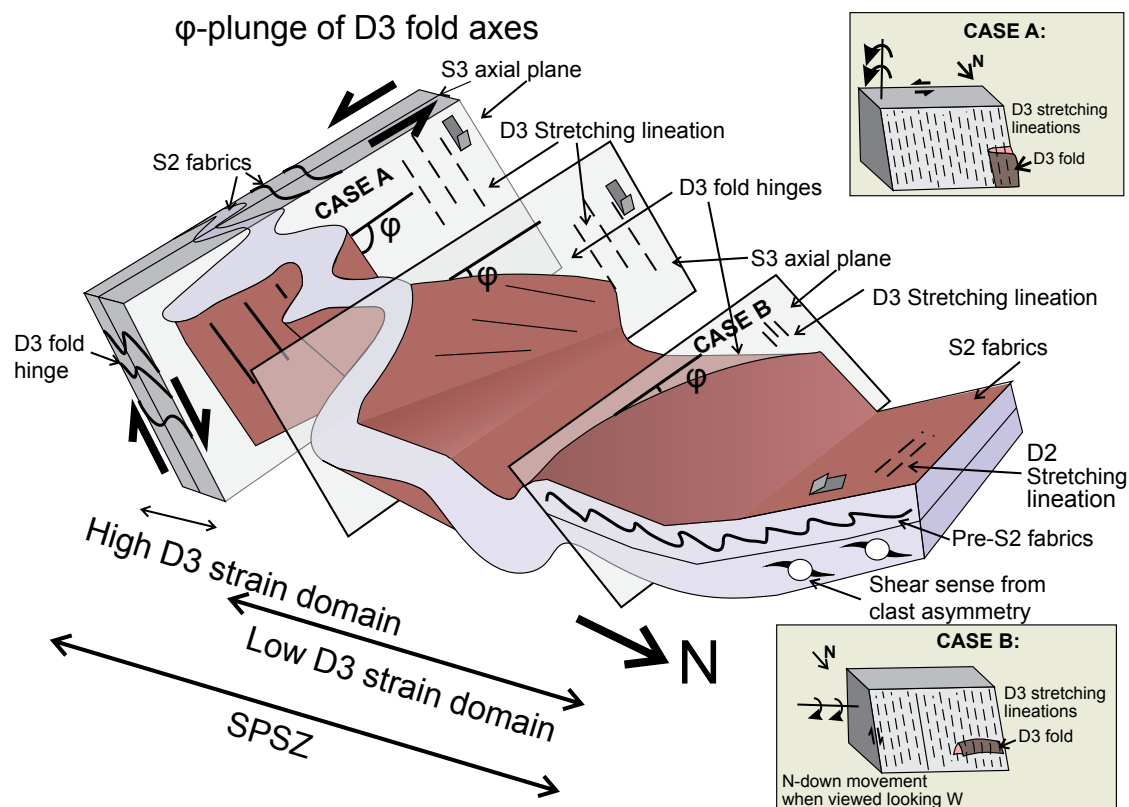


Figure 7. Three-dimensional sketch shows N-S variations in geometry of D_2 folds across the transpressional South Purulia Shear Zone (SPSZ) and southern part of northern domain. Insets to right (modified after Ghosh et al., 2003) explain geometry of D_3 folds in relation to dominant movement sense and stretching lineation within the SPSZ. ϕ is pitch of fold hinge on axial plane of D_2 folds. In the figure, axial plane (S_2) and stretching lineation (L_2) are associated with D_2 deformation, and similarly for S_3 , L_3 , and D_3 . For clarity in presenting details in the figure, normal-sized fonts instead of subscripts are used for designating generations of structural elements.

lenticles in the locally developed melt-hosted D_3 shear zones in foliated granitoids (Fig. 4H) exhibit chessboard microstructure (Fig. 8D); by implication, at least some of the granitoids were still hot ($T > 650^\circ\text{C}$; Kruhl, 1996) during D_3 deformation, but the deformation outlasted solidification of the granitoids.

Although the top-to-the-south thrust-related D_2 structures (recumbent to gently inclined folds and shallowly dipping deformation fabrics; Figs. 7) are shared by the northern domain (Figs. 4B and 4D) and the southern domain (Figs. 4E and 4F), the metamorphic grade of the pre- D_2 fabric in the two domains is different. For example, in the CGC anatectic gneisses, these steeply dipping pre- D_2 structures are defined by alteration of leucosome and mesosome, commonly separated by biotite-rich segregations. This indicates that

upper amphibolite to granulite facies conditions characterized D_{1a} and D_{1b} deformation fabrics in the CGC gneisses. By contrast, the pre- D_2 mineralogy of the mica schists (muscovite, biotite, and chlorite) is characteristic of greenschist facies P - T conditions. Clearly, a sharp difference exists in the pre- D_2 metamorphic grade of the lithodemic units between the northern domain (CGC; pre- D_{1b} high temperature; anatectic conditions) and the southern domain (NSMB; greenschist transitional to amphibolite facies conditions).

The switch from apparent top-to-the-south thrusting (D_2) along shallow planes (S_2) to oblique transpression (D_3) that resulted in dominantly north-down sense of movement along steep north-dipping shear zones (S_3) needs to be explained. Our observations (field photo in Fig. S1 in the

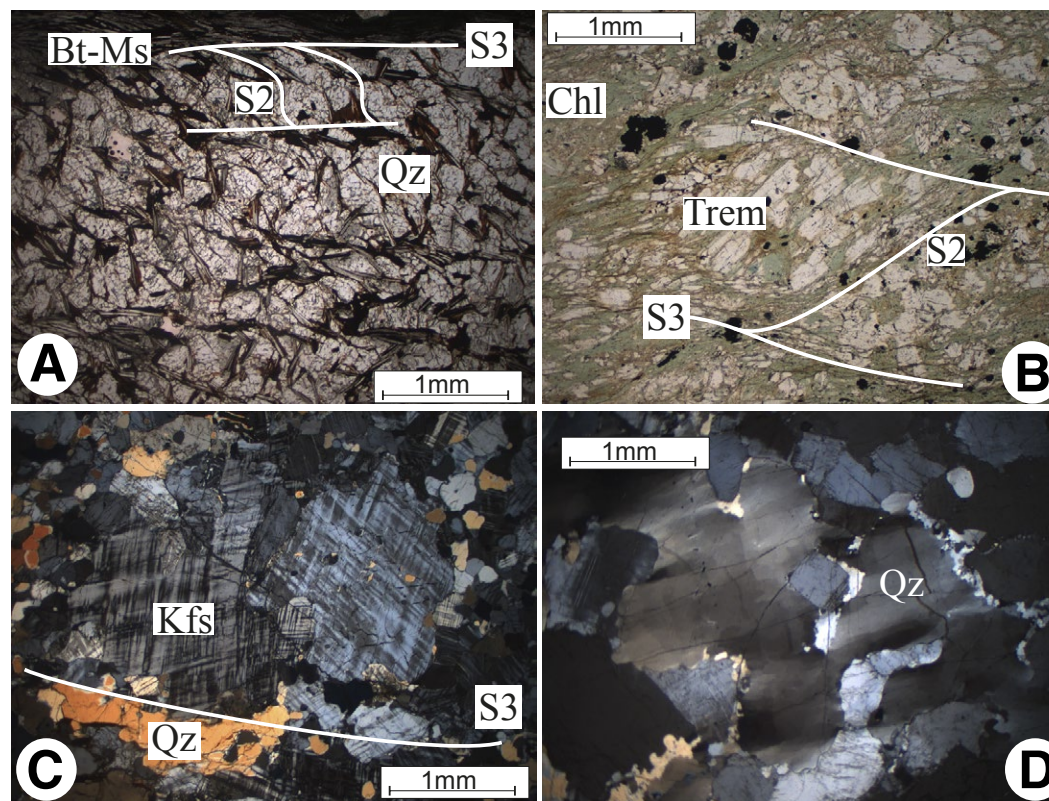


Figure 8. Deformation microstructures. (A) Biotite-muscovite-quartz schists in southern domain showing superposition of S_2 by S_3 fabrics. (B) Chlorite-actinolite bearing mafic schists showing S_2 - S_3 fabrics. (C) Microcline porphyroclasts in granitoid mylonite (D_3 deformations) wrapped by quartz lentils. Feldspar exhibits subgrains and neo-crystallized grains at the margin, but the core is weakly strained. (D) Chessboard microstructure in quartz in post- D_2 melt-hosted D_3 shears in granitoid (same sample as in Fig. 4H). Mineral abbreviations: Ms—muscovite; Bt—biotite; Qz—quartz; Trem—tremolite; Chl—chlorite; Kfs—K-feldspar. For clarity in presenting details in the figure, normal-sized fonts instead of subscripts are used for designating generations of structural elements.

Supplemental Material¹) in the southern flank (S-NSMB) of the meta-igneous rocks of the Dalma Belt show the sense of movement along steeply dipping E-striking S_3 planes is opposite (south-down) to that in the N-NSMB (this study). Taken together, we suggest the Dalma Belt constitutes a syn-contractual extruded crustal domain (Fossen and Tikoff, 1998; Ring and Glodny, 2010) formed synchronously with D_3 oblique N-S crustal shortening. The switch from D_2 to D_3 deformation styles is likely a consequence of reduction in the

rate of northward subduction (D_2) of the southern domain followed by a possible slab break-off that caused the more buoyant over-riding lithosphere to extrude (cf. Schlunegger and Kissling, 2015) relative to the adjacent regions during D_3 crustal shortening.

4. METAMORPHIC P - T CONDITIONS DURING D_2 - D_3 DEFORMATIONS

4.1 Mineral-Textural Relations in Mica Schist WN-47A

In this section, we aim to retrieve the P - T path experienced by rocks during the D_2 thrusting event. We first estimate the metamorphic P - T conditions from mineral thermo-barometry, and subsequently, we retrieve the P - T evolutionary history of the rocks. For this purpose, the greenschist facies mineral assemblages of the phyllites and schists in the southern domain are inadequate for

¹Supplemental Material. Figure S1: Field photo in southern North Singhbhum Mobile Belt showing fabric relations in mica schists interleaved with quartzite and south-down shear sense during D_3 deformation. Text S1: Summary of instrumentation and analytical details for whole-rock geochemistry, laser ablation-inductively coupled plasma-mass spectrometry (LA-ICP-MS) U-Pb zircon dating, and electron probe micro-analysis monazite chemical dating. Table S1: Data table for LA-ICP-MS U-Pb zircon analyses. Text S2: Lithological description and textural characteristics of monazite with dates in Ma. Table S2: Chemical compositions of monazites and spot dates. Figure S2: Probability density plots of monazite dates (<10% error) in individual samples. Please visit <https://doi.org/10.1130/GEOS.S.26858791> to view the supplemental material. Contact editing@geosociety.org with questions.

quantitative *P-T* path reconstruction. Instead, the mineral assemblage in the mica schists in the northern domain are ideally suited for *P-T* estimation of S_2 - S_3 fabric-forming events because these rocks were unaffected by the pre- D_2 high-temperature metamorphic-deformation events experienced by the anatexic basement gneisses.

The mica schists WN-47A (mineral-chemical data in Table 1; analytical protocols in Text S1 [see footnote 1]) and WN-47B (from the same outcrop) consist of staurolite and garnet porphyroblasts that occur in a quartz + muscovite + biotite + chlorite matrix. The staurolite-garnet-bearing mica schists WN-47A and WN-47B possess two prominent schistosity S_2 and S_3 , with an earlier schistosity (pre- S_2) evident in the S_2 intrafolial domains and within staurolite porphyroblasts (Fig. 9A). The S_2 schistosity defined by mica-rich and quartz-rich domains is transposed parallel to unevenly developed S_3 schistosity (Fig. 9A). All three fabrics (pre- S_2 , S_2 , and S_3) are defined by shape-preferred aggregates of muscovite, biotite, and low modal amounts of chlorite; minor amounts of recrystallized K-feldspar and accessory amounts of plagioclase (<0.5 vol%) are dispersed throughout the matrix. Pyrrhotite and ilmenite constitute the opaque phases lodged in the mica-rich domains. In WN-47A, garnet and staurolite together compose ~45 vol% of the rock.

In WN-47A, garnet porphyroblasts are invariably idioblastic and occur both within staurolite porphyroblasts as well as in the mica-quartz matrix exclusive of staurolite (Fig. 9A). The garnets are much smaller in size relative to the considerably larger staurolite porphyroblasts (Fig. 9A). Inclusion trails of elongate quartz grains are common within the staurolite porphyroblasts (Figs. 9B–9D). The inclusion trails (pre- S_2) are straight (Figs. 9B–9D) but are oblique to the both the S_2 and S_3 schistosity (Fig. 9D) that wrap around the porphyroblasts. However, the inclusion-free margins of the staurolite porphyroblasts overgrow both pre- S_2 and S_2 schistosity (Fig. 9D). By contrast, in the garnet porphyroblasts, quartz inclusion trails are either lacking (Fig. 9E) or weakly developed (Figs. 9C and 9D). In the staurolite-hosted garnets, inclusion trails in some garnets are continuous with the inclusion trails in staurolite. However, inclusion trails in some staurolite-hosted garnets are oblique to the straight inclusion trails in staurolite. Small modal amounts of garnet porphyroblasts overgrow the S_3 schistosity and are inferred to be post-tectonic with respect to S_3 (Figs. 9F and 9G). But post- S_3 staurolite is not observed. Also, staurolite is not included within garnet porphyroblasts. The textural relations suggest that garnet growth continued from pre- S_2 (Fig. 9) to post- S_3 (Figs. 9F and 9G); by contrast, staurolite growth initiated pre- S_2 (Figs. 9A and 9B) but growth was impeded prior to S_3 . Thus, both staurolite and garnet grew contemporaneously between the pre- S_2 and post- S_2 fabric-forming events (Figs. 9B and 9C).

The idiomorphic faces of the garnets hosted within staurolite porphyroblasts are not embayed at the contact with the host staurolite grains (Figs. 9B–9D). Though the porphyroblast-matrix relations suggest growth of staurolite and most of the garnets are contemporaneous, the perseverance of idioblastic garnet within staurolite indicates that both the minerals formed independent of each other at the expense of muscovite, biotite, and chlorite. In other words, staurolite did not form at the expense of garnet; i.e., the garnets were enclosed

by the larger staurolite grains. In rare instances, both garnet and staurolite porphyroblasts are replaced by randomly oriented chlorite-muscovite aggregates (Fig. 9).

The almandine-rich garnets enclosed within staurolite (Grt 1, Figs. 10A–10D) exhibit a rimward increase in Fe (weakly reddish in the core), Mg, and Ca and a decrease in Mn from the core to the rim. The almandine (Alm), pyrope (Prp), grossular (Grs), and spessartine (Sps) phase components of the garnet vary accordingly from $Alm_{78}Prp_6Grs_6Sps_{10}$ in the core to $Alm_{81}Prp_9Grs_6Sps_2$ in the rim. The composition of garnet at the margin of the host staurolite porphyroblasts (Grt 2, Figs. 10A–10D) varies from $Alm_{77}Prp_7Grs_6Sps_3$ in the core to $Alm_{81}Prp_9Grs_6Sps_2$ at the rim. By comparison, chemical zoning in garnets within the matrix and occurring exclusive of staurolite is less pronounced; e.g., core composition is $Alm_{80}Prp_9Grs_6Sps_5$, and rim composition is $Alm_{81}Prp_8Grs_6Sps_2$ (Grt 3, Figs. 10A–10D). Staurolite porphyroblasts are chemically homogeneous, with X_{Fe} varying between 0.83 and 0.86. In biotite, X_{Fe} lies in the range 0.53–0.55, and TiO_2 contents vary from 1.32 to 1.81 wt% oxide. Si contents in muscovite vary in the range 2.97 and 3.09 atoms per formula unit (apfu). Muscovite with Si contents >3 apfu are weakly phengitic. But no systematic variation in phengite component in muscovite from the two schistosity is noted. (Fe^{2+} + Mg) in muscovite varies between 0.18 and 0.26 apfu, and TiO_2 contents are in the range 0.23–0.41 wt%. Chlorite has X_{Fe} values ranging from 0.49 to 0.52. The albite contents in plagioclase (oligoclase-andesine) vary between 0.66 and 0.70 mol%. No systematic compositional variations in biotite, muscovite, or chlorite are observed in the two different schistosity and in the different textural domains.

4.2 Mineral Thermo-Barometry

P-T conditions were obtained using several thermometers in samples WN-47A and WN-47B (Fig. 11A). Temperatures estimated from the garnet-staurolite thermometer of Perchuk (1989) are 470–540 °C (all *T* values are rounded to the nearest tens) at 4 kbar pressure for garnet core–staurolite pairs; the garnet rim–staurolite pairs yielded similar temperature (510–540 °C) at the same pressure. The garnet-biotite temperatures were obtained using different formulations (Ferry and Spear, 1978; Bhattacharya et al., 1992; Holdaway et al., 1997; Holdaway, 2000; Kaneko and Miyano, 2004). Garnet core and matrix biotite pairs yield temperatures in the range of 470–580 °C at 5 kbar pressure; comparable temperatures are obtained from garnet rims and matrix biotite pairs (480–590 °C) at the same pressure. Pressure estimates were obtained from WN-47B for the assemblage garnet–muscovite–plagioclase (Ab_{70})–quartz using the barometer of Wu and Zhao (2006). Estimated pressures are in the range of 4.0–4.4 kbar at *T* = 500 °C using garnet core compositions; equilibrium pressure (4.4–4.9 kbar) computed using garnet rim compositions at the same temperature is comparable. In addition to the above thermo-barometers, the empirically determined biotite-muscovite-chlorite thermo-barometer (Powell and Evans, 1983) was applied (Fig. 11A). The muscovite, biotite, and chlorite

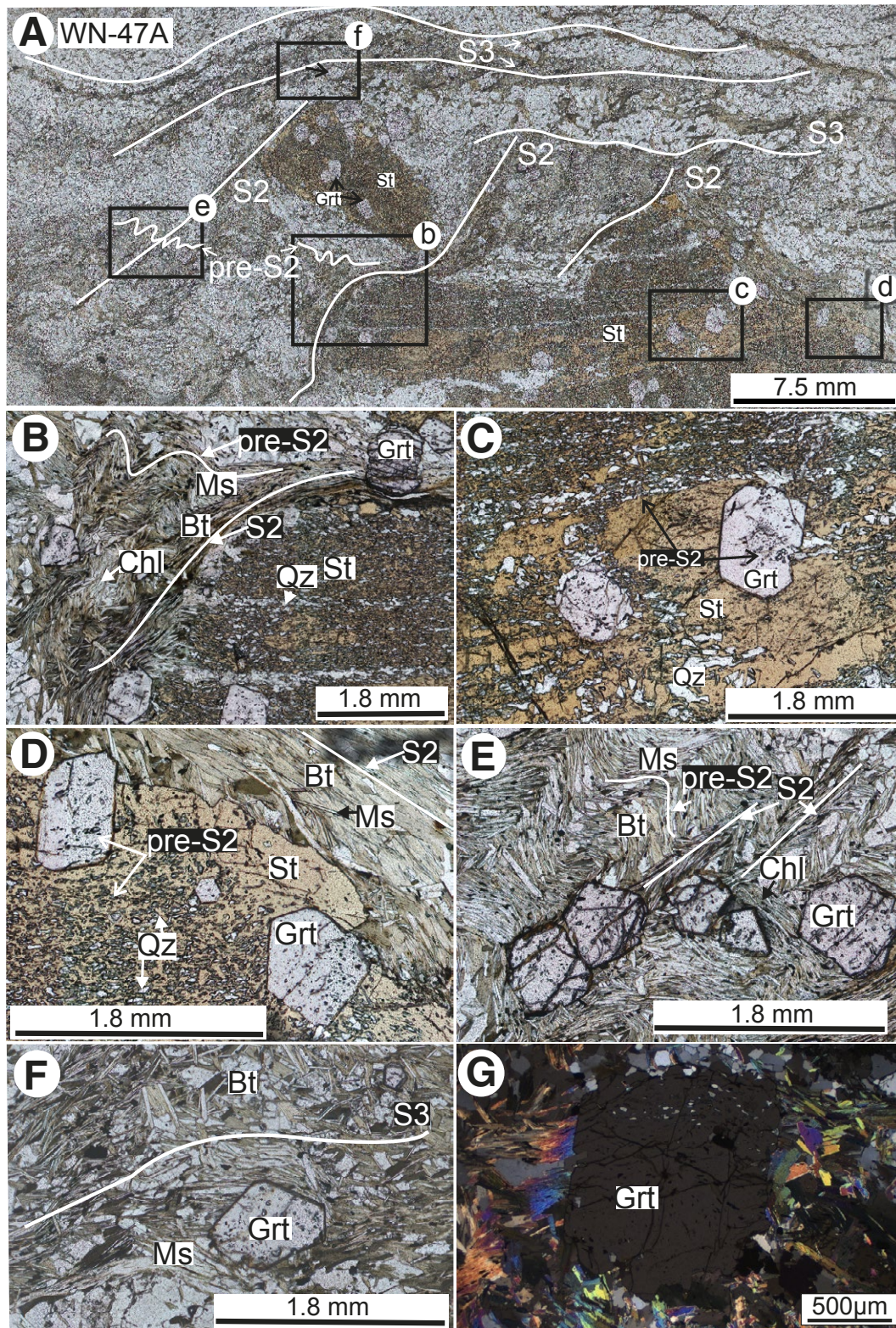


Figure 9. Plane-polarized microscopy of porphyroblast-matrix relations in sample WN-47A (A-F) and crossed-polar image in WN-47B (E and G). (A) Image of full thin section. Arrows show garnet porphyroblasts. Boxes show locations of photos B-F. (B) Straight pre-S₂ inclusion trails in staurolite terminate against warping S₂ schistosity. (C) Idioblastic garnets hosted within staurolite porphyroblast. Inclusion trails in staurolite are continuous within garnet (arrow). (D) Inclusion-free rim of staurolite overgrows both pre-S₂ and S₂ schistosity. Idioblastic garnet is included within staurolite. (E) Inclusion-free garnet porphyroblasts overgrowing both pre-S₂ and S₂ schistosity. (F) Idioblastic garnet overgrowing warping muscovite-biotite-defined S₃ schistosity. (G) Post-S₃ garnet porphyroblast in WN-47B (polarizer and analyzer are not orthogonal). Note quartz inclusion trails in garnet are continuous with external muscovite-biotite-defined S₃ schistosity (top left to bottom right). Note small V-shaped divergence of S₃ fabric in the left of the garnet porphyroblast. This implies that part of the garnet is pre-tectonic with respect to S₃. Mineral abbreviations: St—staurolite; Grt—garnet; Bt—biotite; Chl—chlorite; Ms—muscovite; Qz—quartz. For clarity in presenting details in the figure, normal-sized fonts instead of subscripts are used for designating generations of structural elements.

compositions (Table 1) were used to determine the $\ln K_d$ (as in Powell and Evans, 1983) for the previously mentioned reaction equilibrium. The P - T loci for the equilibria corresponding to the range of Si-in-muscovite values between 3.04 and 2.97 apfu are shown in Figure 11A. The P - T estimates obtained using the formulation of Powell and Evans (1983) match with those obtained from the intersections of the staurolite-garnet and biotite-garnet thermometers and the barometer proposed by Wu and Zhao (2006) (Fig. 11A).

4.3 Pseudosection Modeling and P - T Path Reconstruction

For P - T path reconstruction, the mica schist WN-47A is favored over WN-47B for it contains accessory amounts of ilmenite. These ilmenite (FeTiO_3) grains are stoichiometric in composition, with negligible contents of hematite (Fe_2O_3), geikielite (MgTiO_3), and pyrophanite (MnTiO_3) in solid solution. This negligible Fe_2O_3 content in ilmenite minimizes the effect of oxygen fugacity [$f(\text{O}_2)$] in fluid in reconstructing the metamorphic P - T pseudosection modeling. The bulk-rock composition of WN-47A is approximated to the TiO_2 - MnO - Na_2O - CaO - K_2O - FeO - MgO - Al_2O_3 - SiO_2 - H_2O (Ti-MnNCKFMASH) system. The Ti-MnNCKFMASH P - T pseudosection (Figs. 11B and 11C) was constructed using PERPLEX 7.1.0 (database: hp62ver.dat) software (Connolly, 2005). For the P - T range, the following phases and phase components (in square brackets) were adopted from the software database: garnet, Gt [alm, py, gr, sps]; chloritoid, Ctd [fctd, mctd, mnctd]; staurolite, St [fst, mst, mnst]; cordierite, Crd [crd, fcrd, hcrd, mnctd]; biotite, Bio [ann, phl, east, mnbi]; chlorite, Chl [ames, clin, daph, mnchl]; mica, Ms [mu, pa, cel, fcel]; plagioclase, Pl [abh, an]; K-feldspar, Kfs [San]; clinzoisite [Zo]; andalusite [And]; sillimanite [Sil]; kyanite [Ky]; quartz [Qz]; rutile, [Rt]; ilmenite, [Ilm]; margarite, [Ma]. Quartz and H_2O were considered to be in excess. The solution models are adopted from Holland and Powell (2001) for garnet, staurolite, chloritoid, and melt; White et al. (2014) for chlorite, cordierite, and muscovite; White et al. (2007) for biotite; Newton et al. (1981) for plagioclase; and Waldbaum and Thompson (1968) for K-feldspar. These solution models and the ideal solution model for talc (T) were used from the solution_model_690.dat file from the software for construction of the pseudosection.

The bulk-rock composition (WN-47A) for which the P - T was constructed in the Ti-MnNCKFMASH system is as follows (in weight percent): $\text{SiO}_2 = 53.8$, $\text{TiO}_2 = 0.71$, $\text{Al}_2\text{O}_3 = 23$, $\text{FeO} = 12.7$, $\text{MgO} = 2.62$, $\text{MnO} = 0.15$, $\text{CaO} = 0.52$, $\text{Na}_2\text{O} = 0.42$, $\text{K}_2\text{O} = 3.95$, and H_2O (loss on ignition) = 3.08 (total = 101.00). Sample preparation and analytical procedure for whole-rock analysis is outlined in Text S1 (see footnote 1). The phase topologies obtained in the P - T window, 3.5–9.0 kbar and 400–700 °C, are shown in Figure 11B. The P - T estimates obtained from conventional mineral thermo-barometry (red box in Fig. 11A) are shown as a white transparent field in Figure 11B for reference. The fields of interest comprising the peak mineral assemblage (St-Grt-Ms-Bt-Chl) of the mica schist sample WN-47A lie within the calculated P - T range. The P - T window is thus narrowed down to 4.6–9.0 kbar and 450–650 °C for better representation in

Figure 11C, and contours for X_{Fe} , X_{Mn} , and X_{Ca} in Grt, X_{Fe} in St, Grt volume percent, and St volume percent are shown.

Thus, in the phase fields of interest consisting of staurolite-muscovite-biotite-garnet-chlorite, a P - T path for pre- S_2 to post- S_2 metamorphism is constructed using the isopleths for X_{Fe} , X_{Mn} , and X_{Ca} values in garnet varying from the core ($\text{Alm}_{78}\text{Prp}_6\text{Grs}_6\text{Sps}_{10}$) to the rim ($\text{Alm}_{81}\text{Prp}_9\text{Grs}_8\text{Sps}_2$) consistent with increasing X_{Fe} and X_{Ca} and decreasing X_{Mn} in garnet (Fig. 11C). The P - T path also coincides with the general direction of increasing volume percent of garnet and staurolite and is sub-parallel to the X_{Fe} isopleths in the weakly zoned staurolite (Fig. 11C). Thus, an overall loading P - T path is obtained from the pre- S_2 to post- S_2 growth of garnet and staurolite (Fig. 11C). Along the P - T path, the isopleths of the theoretical mole fraction values in garnet and staurolite (Fig. 11C) deviate slightly from the measured ranges of mole fractions of the phase components in the minerals (Fig. 10E; Table 1). This is expected because the mineralogy across the layering in sample WN-47A (Fig. 9A) is not uniform, and therefore the composition of the reaction volume (Dunkley et al., 1999; Nasipuri et al., 2009) at the site where a porphyroblast grows varies. Further, in multiply deformed rocks, the reaction volumes are modified by subsequent fabric-forming events as the minerals continue to grow. Also, as $X(\text{H}_2\text{O})$ in the fluid in the computations is assumed to be 1, reduction in H_2O mole fraction is likely to shift the phase topologies and the isopleths, without distorting their geometries, to lower P - T conditions (cf. Rekha and Bhattacharya, 2014). This would cause the reconstructed P - T path to shift to lower metamorphic grade, but the geometry of the reconstructed near-isothermal loading path would be unlikely to change. Thus, the metamorphic P - T path (Fig. 11C) constructed using the bulk-rock composition is semiquantitative (Rekha and Bhattacharya, 2014).

It is evident (Fig. 11C) that the pre- to post- S_2 mineral paragenesis in the schist is consistent with mid-crustal near-isothermal loading. Both the D_2 and D_3 deformations are contractional in nature, but conceivably, movement along the steeply dipping D_3 fabrics could not have produced prograde loading; instead, the top-to-the-south D_2 thrusting would have led to loading (Fig. 7). This implies that the P - T path (Fig. 11C) was a consequence of top-to-the-south D_2 thrusting, which necessitates that the northern domain was the over-riding plate during D_2 crustal shortening.

5. GEOCHRONOLOGY

In this section, we ascertain the timing of different events based on laser ablation inductively coupled plasma mass spectrometry (LA-ICP-MS) U-Pb analyses of zircons in five samples (WN-4A, WN-43, WN-63, WN-84, and WN-138A) and Th-U-Pb (total) chemical dating of monazite in nine samples (WN-22A, WN-26A, WN-27, WN-30, WN-84, WN-86, WN-140, YD-7A, and YD-7B) using electron probe micro-analysis (EPMA) (Montel et al., 1996). The samples WN-47A and WN-47B used for P - T estimation contained neither monazite nor zircon. The analytical protocols and instrumental conditions for U-Pb analyses using LA-ICP-MS and monazite dating using EPMA are summarized in Text S1

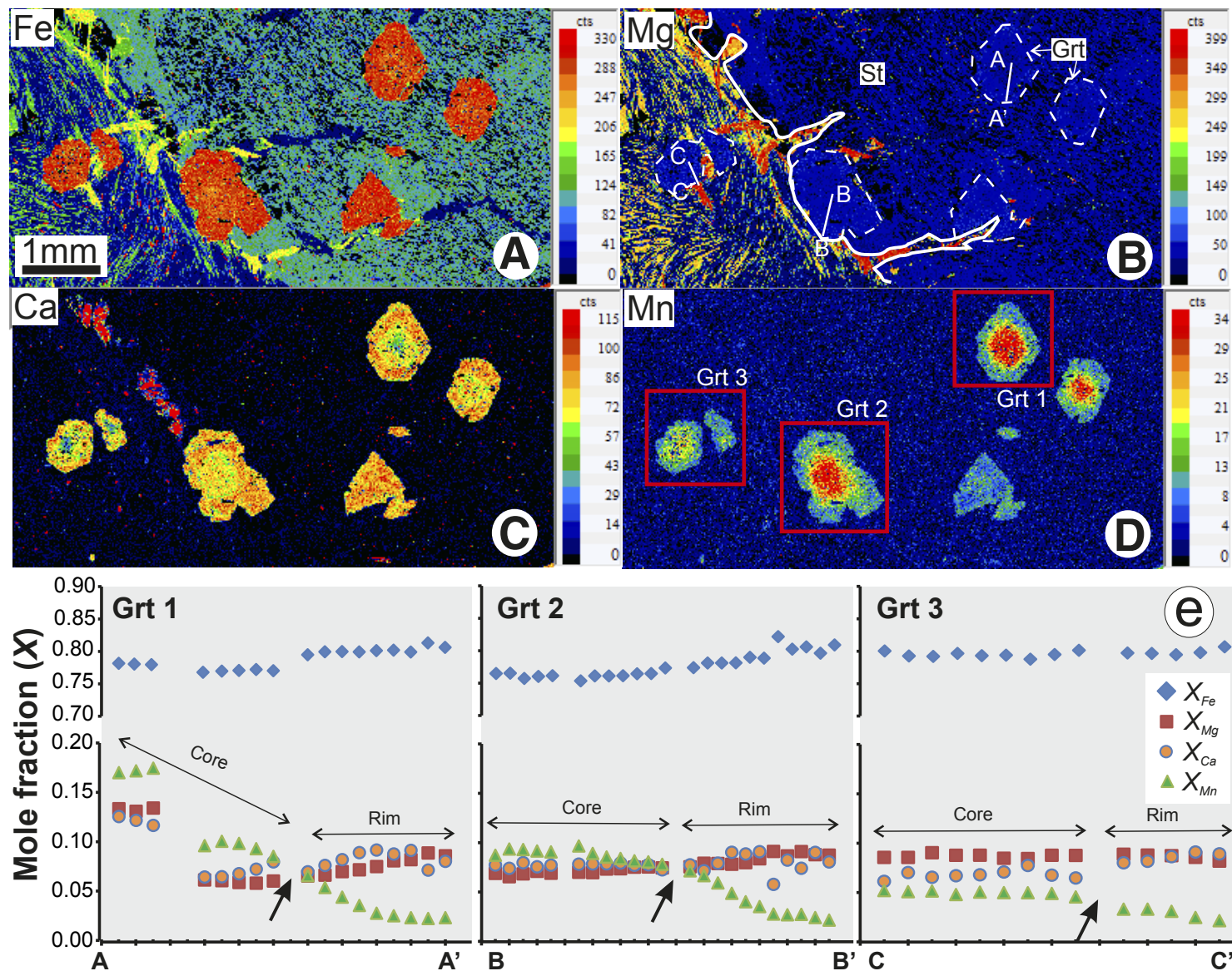


Figure 10. (A–D) X-ray element maps of Fe (A), Mg (B), Ca (C), and Mn (D) variations in garnet porphyroblasts, e.g., within staurolite (Grt 1 and 2) and in the micaceous matrix (Grt 3). In B, white line demarcates margin of staurolite grain to the right, and white broken lines outline garnet grains. (E) Core-to-rim variations (along profile lines shown in B) of mole fractions X_i where $i = \text{Fe, Mg, Mn, and Ca}$ in garnet porphyroblasts, e.g., $X_{Ca} = \text{Ca}/(\text{Ca} + \text{Fe} + \text{Mn} + \text{Mg})$. Variations between the core and rim indicated by bold black arrows coincide with downward inflection of X_{Mn} . Mineral abbreviations: St—staurolite; Grt—garnet. Vertical scales in panels A–D denote the intensities of elements in counts per second.

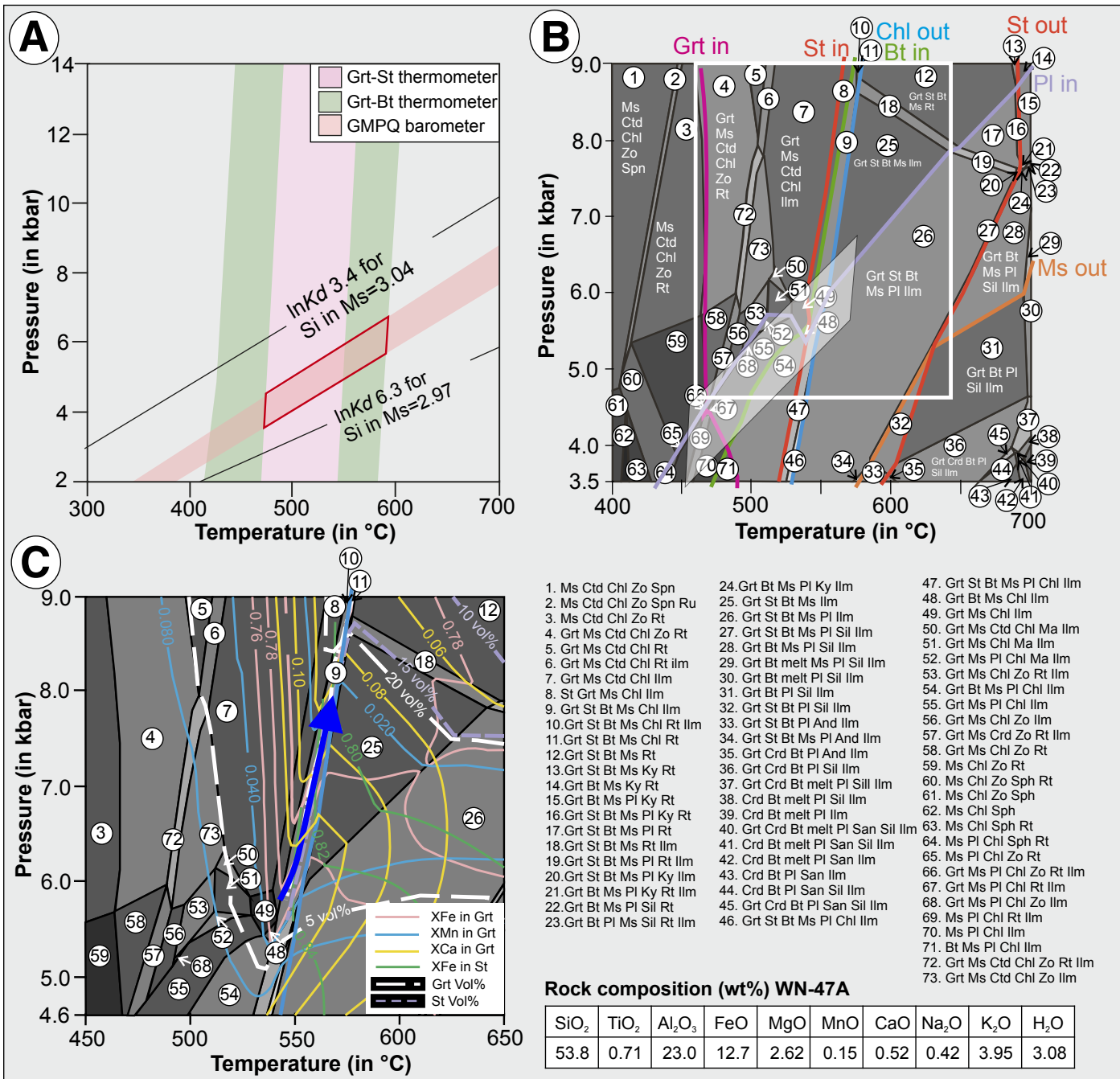


Figure 11. (A) Pressure-temperature (P - T) estimates obtained in mica schist WN-47A using different thermo-barometers (see text). $\ln K_d$ is computed as in Powell and Evans (1983). GMPQ is the acronym for garnet-muscovite-plagioclase-quartz barometer (Wu and Zhao, 2006). Si in Ms is the Si content in muscovite per formula unit (Table 1). (B) P - T pseudosection phase topology (see text). Shaded parallelogram corresponds to the preferred P - T conditions obtained from thermo-barometry indicated by the parallelogram outlined by the red line in (A). (C) Volume percent of staurolite and garnet is shown; also shown are X_{Fe} , X_{Ca} , and X_{Mn} isopleths in garnet and X_{Fe} isopleth in staurolite. Inferred P - T path (blue arrow) is consistent with growth of both staurolite and garnet (Fig. 8A) and variations in garnet zoning (Fig. 10). Abbreviations of mineral phases are same as used in solution models adopted for constructing the P - T pseudosection (see section 4.3).

(see footnote 1). Both zircon and monazite were dated in WN-84 (Ranibandh granite) to check date compatibility between the two dating methods. Brief lithological-mineralogical details, locations, and dates of the samples are summarized in Table 2.

5.1 U-Pb Zircon Dating

U-Pb (zircon) dating was performed on granitoid mylonites (WN-4A, WN-43, and WN-63) and anatectic quartzofeldspathic gneiss (WN-138A) from the northern domain and the Ranibandh granite (WN-84) in the southern domain. The morphologies and internal structures of zircons in the samples are provided in Figure 12; U-Pb zircon dates are in Figure 13 (analytical values are in Table S1). Dates are reported with (given in italics within parentheses) and without propagation of systematic uncertainties (Horstwood et al., 2016) at the 2σ level in the text.

5.1.1 Sample WN-4A

Zircons in sample WN-4A are prismatic, with long axes varying between 100 and 300 μm and axial ratios between 2 and 5 (Fig. 12A). Cathodoluminescence (CL) images exhibit internal CL dark cores with thin CL bright overgrowths. The

internal cores exhibit patchy to nebulous zoning and are embayed along their margins; a few grains, however, show magmatic oscillatory zoning (Fig. 12A). Thirty spots were ablated across different domains in twenty-three grains; eight of them yielded a concordia date of 1569 ± 6 (13) Ma (*n* = 8; mean square weighted deviation [MSWD] = 0.22) (Fig. 13A). An overwhelming number of concordant spots are from cores (Fig. 12A) having variable Th/U ratios (0.16–1.56; Table S1). Discordant spots are obtained from cores as well as rims in the zircon grains; together with 14 other spots, they define a discordia with an upper intercept at 1569 ± 13 (17) Ma (*n* = 22; MSWD = 1; Figs. 13A and 13B) coherent with the concordia date.

5.1.2 Sample WN-43

In the post-D₂ granitoid traversed by locally developed E-striking sub-vertical sinistral D₃ shear zones, zircons are short, prismatic, and characterized by well-defined core-rim textures on CL images (Fig. 12B). The long axes of the zircon grains in sample WN-43 vary between 80 and 200 μm and axial ratios within 1–2. Some of the zircon grains exhibit magmatic oscillatory zoning; some grains have a recrystallized core with patchy nebulous zoning overgrown by a thick homogenous rim of CL bright zone (Fig. 12B). Thirty spots were analyzed in twenty-two grains from this sample. Most of the spots ablated have yielded

TABLE 2. MINERAL ASSEMBLAGES, LOCATIONS, AND DATES OF ZIRCON- AND MONAZITE-DATED SAMPLES

Sample	Location		Domain	Lithology	Mineralogy	Spots analyzed	Dates obtained*
	Latitude	Longitude					
Zircon dating							
WN-4A	22°59.989'N	86°38.293'E	Northern	Steeply dipping ESE-striking (S ₂) foliated granitoid	Qz, Pl, Kfs, Bt, Ms, Zrn, Ap	30 spots, 23 grains	1569 ± 6 (13) Ma (conc.)
WN-43	23°21.117'N	86°26.978'E	Northern	Shallowly dipping (S ₂) foliated granitoid	Kfs, Pl, Bt, Ap, Ilm, Zrn	30 spots, 22 grains	1020 ± 4 (10) Ma (conc.)
WN-63	23°10.866'N	86°36.634'E	Northern	NNE-striking foliated granitoid	Qz, Kfs, Pl, Ilm, Ap, Zrn	30 spots, 22 grains	1670 ± 5 (15) Ma, 1601 ± 4 (12) Ma (conc.)
WN-138A	23°12.083'N	86°29.695'E	Northern	Poly-deformed anatectic quartzofeldspathic gneiss	Qz, Kfs, Pl, Bt, Ap, Ilm, Zrn	30 spots, 24 grains	1762 ± 31 (32) Ma, 1569 ± 13(16) Ma (UI)
WN-84	22°49.484'N	86°37.730'E	Southern	Shallowly dipping foliated Ranibandh granitoid	Qz, Kfs, Pl, Ms, Bt, Ilm, Ap, Mnz, Zrn	30 spots, 14 grains	1884 ± 13 (16) Ma, 1670 ± 12 (16) Ma (UI)
Monazite dating							
YD-7A	23°12.103'N	86°05.099'E	Northern	Crenulated (D ₃ folds), shallowly dipping (S ₂) muscovite schist	Qz, Ms, Bt, Chl, Pl, Ap, Mnz	22 spots, 5 grains	916 ± 14 Ma
YD-7B	23°12.103'N	86°05.099'E	Northern	Crenulated (D ₃ folds), shallowly dipping (S ₂) muscovite schist	Qz, Ms, Bt, Chl, Pl, Ap, Mnz, Zrn	39 spots, 6 grains	911 ± 16 Ma, 1011 ± 23 Ma
WN-22A	23°10.700'N	86°20.821'E	Northern	Shallowly dipping (S ₂) anatectic quartzofeldspathic gneiss	Qz, Kfs, Pl, Bt, Ap, Ilm, Mnz	28 spots, 8 grains	962 ± 13 Ma
WN-26A	23°06.171'N	86°08.852'E	Northern	ESE-striking (S ₃) poly-deformed anatectic quartzofeldspathic gneiss	Qz, Kfs, Pl, Bt, Ap, Zrn, Mnz	22 spots, 5 grains	924 ± 52 Ma, 1012 ± 19 Ma
WN-140	23°11.518'N	86°29.534'E	Northern	NNE-striking steeply dipping anatectic gneiss	Qz, Kfs, Pl, Bt, Ap, Ilm, Mnz	15 spots, 6 grains	904 ± 26 Ma, 1028 ± 110 Ma
WN-27	23°06.467'N	86°06.952'E	Southern	ESE-striking steeply dipping (S ₃) muscovite schist	Qz, Ms, Pl, Kfs, Mnz	37 spots, 7 grains	874 ± 15 Ma, 956 ± 15 Ma, 1045 ± 12 Ma
WN-30	23°06.105'N	86°03.890'E	Southern	ESE-striking steeply dipping (S ₃) biotite-muscovite schist	Qz, Ms, Bt, Grt, Pl, Czo, Ilm, Ap, Mnz	30 spots, 8 grains	873 ± 23 Ma, 953 ± 12 Ma, 1023 ± 23 Ma
WN-84	22°49.484'N	86°37.730'E	Southern	Foliated Ranibandh granitoid	Qz, Kfs, Pl, Ms, Bt, Ilm, Ap, Mnz, Zrn	53 spots, 7 grains	1290 ± 77 Ma, 1431 ± 37 Ma, 1572 ± 31 Ma, 1717 ± 34 Ma
WN-86	22°50.621'N	86°43.013'E	Southern	Shallowly dipping (S ₃) garnet-bearing muscovite schist	Qz, Bt, Ms, Ilm, Tur, Mnz	26 spots, 6 grains	1303 ± 14 Ma

Notes: Mineral abbreviations (after Whitney and Evans, 2010): Qz—quartz; Pl—Plagioclase; Kfs—K-feldspar; Bt—biotite; Ms—muscovite; Zrn—zircon; Ap—apatite; Ilm—ilmenite; Mnz—monazite; Chl—chlorite; Grt—garnet; Czo—clinozoisite; Tur—tourmaline.

*conc.—concordant date; UI—upper intercept of discordia for zircon dates. Monazite dates are weighted mean dates. All errors are 2σ. The error values shown in italics are explained in the text and in Text S1 (see footnote 1 in text).

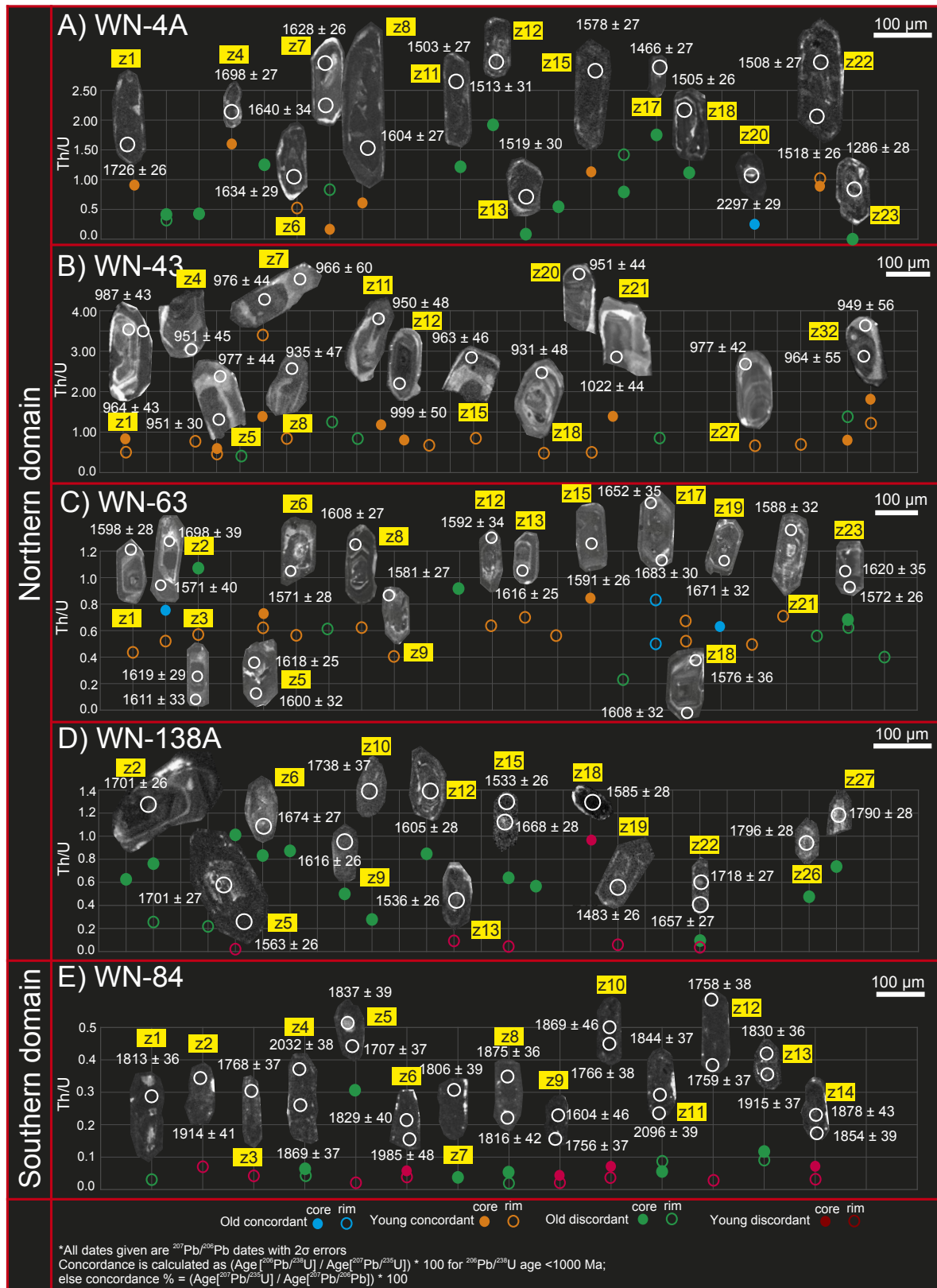


Figure 12. Cathodoluminescence images of morphology and internal structures of zircons in granitoids and gneisses in northern (A–D) and southern (E) domains; laser ablation inductively coupled plasma mass spectrometry U–Pb $^{207}\text{Pb}/^{206}\text{Pb}$ dates (in Ma) with 2σ errors are keyed to the images (white circles within zircon grains). Value of Th/U ratio (filled and unfilled colored circles) for the analyzed spot are shown along y-axes; x-axis position of vertical lines corresponds to “number” of analyzed spot in Table S1 (see text footnote 1). Some Th/U ratios cannot be vertically traced to an analyzed spot (white circle) because not all zircon-dated grains in a rock are shown, but full analytical data are provided in Table S1. Note that for each sample, vertical line to the left (y-axis itself) corresponds to spot number “zero”; i.e., no zircon grains are shown along y-axis. In addition, grain numbers are labeled in yellow highlight.

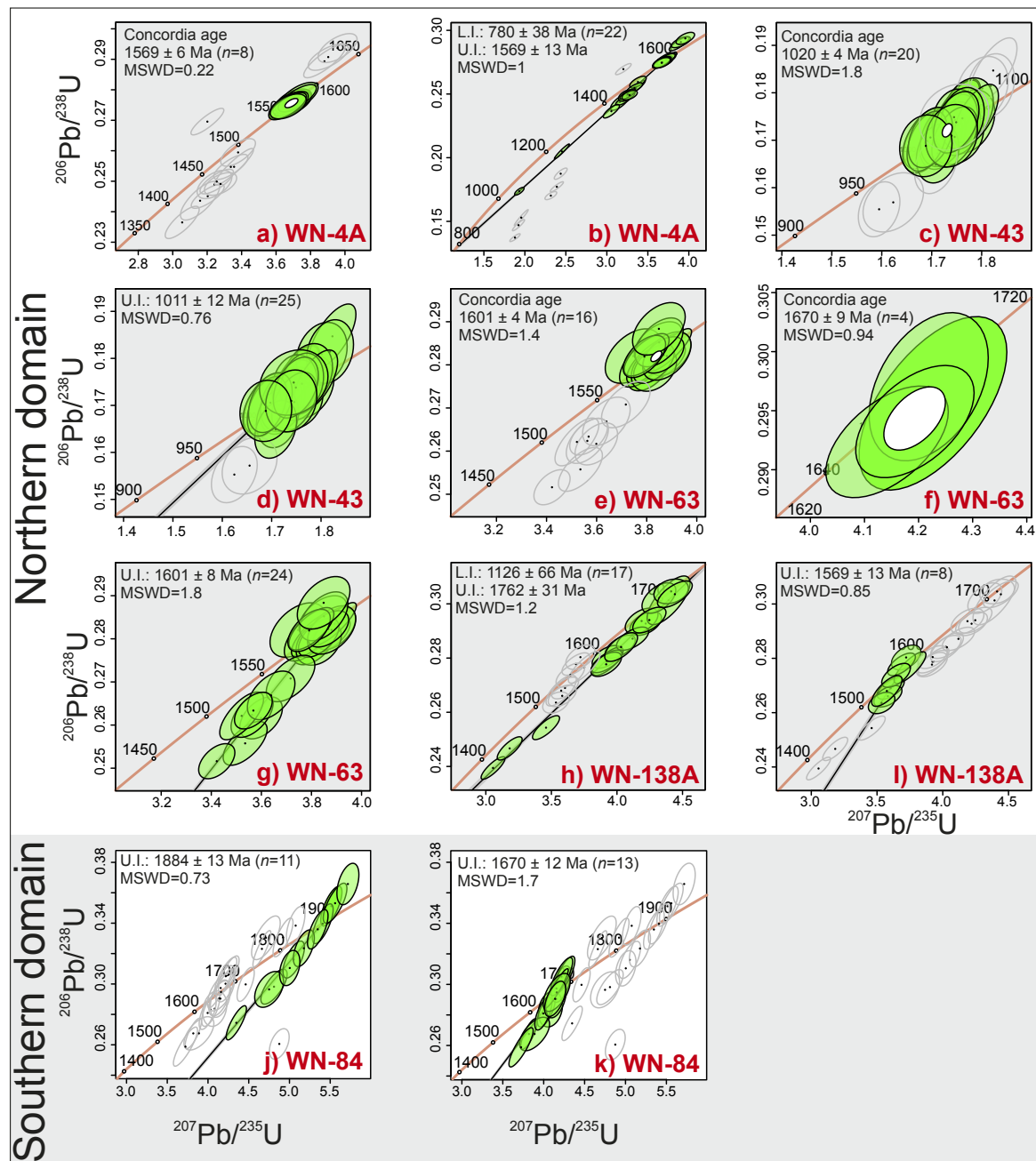


Figure 13. U-Pb Wetherill diagrams for the five samples of granitoids and gneisses. Green ellipses were used for date calculation. MSWD—mean square weighted deviation; L.I.—lower intercept; U.I.—upper intercept.

concordant dates at 1020 ± 4 (10) Ma ($n = 20$; MSWD = 1.8; Fig. 13C). Adding five spot analyses defines a discordia with an upper intercept at 1011 ± 12 (15) Ma ($n = 25$; MSWD = 0.76; Fig. 13D). The concordant spots are from both the cores and rims of the zircon grains (Fig. 12B); Th/U ratios vary between 0.51 and 3.41 (Fig. 12B; Table S1).

5.1.3 Sample WN-63

The rock sampled by sample WN-63 is a shallowly dipping (S_2 fabric) foliated granitoid. Zircon grains exhibit well-defined core-rim textures in CL images; the grains are prismatic with prominent magmatic oscillatory zoning (Fig. 12C). The long axes of these grains are between 80 and 200 μm , and the axial ratios are between 1 and 2. Most grains show oscillatory magmatic zoning and have euhedral shapes, but in some grains, the cores with darker CL response (relative to rims) have embayed margins (Fig. 12C). Thirty spots were analyzed in twenty-two grains; of these, twenty spot analyses define two concordant populations: at 1670 ± 9 (15) Ma ($n = 4$; MSWD = 0.94) and at 1601 ± 4 (12) Ma ($n = 16$; MSWD = 1.4; Figs. 13E and 13F). A discordia is also defined with eight additional spots analyses with an upper intercept at 1601 ± 8 (13) Ma ($n = 24$; MSWD = 1.8; Fig. 13G). The analyzed spots belonging to the older concordant date population (1670 ± 9 Ma) are from (1) anhedral cores of zircon grains that have younger zoned rims and (2) zircon grains that exhibit oscillatory zoning and are euhedral in shape (Fig. 12C). Spot analyses of the younger concordant date population (1601 ± 4 Ma) are obtained in the rims of zircon grains, with a single exception, i.e., zircon 18 (Table S1), which shows uniform growth zoning across the grain (Fig. 12C). All concordant spot analyses have Th/U ratios between 0.42 and 0.70 (a discordant spot analyses has Th/U ratio as high as 1.07; zircon 3, Fig. 12C).

5.1.4 Sample WN-138A

The anatectic quartzofeldspathic gneiss exhibits D_2 recumbent folds. The zircon grains in sample WN-138A are idiomorphic to sub-idiomorphic; the long axes of the grains range between 100 and 200 μm (Fig. 12D). The grains display complex internal structures, commonly have multiple cores showing oscillatory zones, and are rimmed by un-zoned to weakly zoned mantles with dark CL responses (Fig. 12D). The cores are resorbed, and the chemical zones in the cores terminate against the oscillatory zones in the mantles. Thirty spot analyses from the cores and rims of zircon grains yielded two discordia lines: an older discordia defined by seventeen spot analyses with an upper intercept at 1762 ± 31 (32) Ma ($n = 17$; MSWD = 1.2; Fig. 13H) and a younger discordia defined by eight spot analyses with an upper intercept at 1569 ± 13 (15) Ma ($n = 8$; MSWD = 0.85; Fig. 13I). The Th/U ratios in the analyzed spots lie between 0.04 and 1.09 (Fig. 12D; Table S1). The older discordant spots, with Th/U ratios >0.1 , are restricted to the cores of the grains (Fig. 12D). Zircon 18, which has

no overgrowth or rim, has a single date that belongs to the younger discordia with Th/U ratio >0.1 (Fig. 12D). By contrast, the younger discordant spots in the rims of grains have Th/U ratio <0.1 (Fig. 12D).

5.1.5 Sample WN-84

The rock sampled by sample WN-84 is a shallowly dipping (S_2) foliated granitoid near Ranibandh. The foliation (S_3) is defined by muscovite aggregates. The zircon grains are few but large, with long axes between 100 and 200 μm (Fig. 12E). CL images of 14 grains exhibit the zircons to be euhedral to subeuhedral in shape, with well-developed prismatic faces and pyramidal terminations. The grain interiors majorly show CL dark response; either oscillatory zoning is lacking, or zoning is patchy and nebulous. In all, 30 spots were analyzed from the grain interiors and margins. Th/U ratios of nearly all ablated spots are <0.1 (Fig. 12E); the exception is one of the grains in the older discordia (see the following sentence), with Th/U ratio = 0.31 (Fig. 12E; Table S1). Two discordia lines arise from the analyzed spots; an older discordia is defined with an upper intercept at 1884 ± 13 (16) Ma ($n = 11$; MSWD = 0.73; Fig. 13J), and a younger discordia is defined with an upper intercept at 1670 ± 12 (16) Ma ($n = 13$; MSWD = 1.7; Fig. 13K).

5.2 Monazite Chemical Dating

Three anatectic quartzofeldspathic gneisses (WN-22A, WN-26A, and WN-140) and two muscovite schists (YD-7A and YD-7B) from the northern domain and three muscovite schists (WN-27, WN-30, and WN-86) and a sample from the Kuilapal granite (WN-84) from the southern domain were dated (summary in Table 2). The textural characteristics of representative monazites, chemical compositions of monazites and chemical dates of individual samples, and domain-wise probability density plots of monazites (Isoplot software; Ludwig, 2012) are in Text S2, Table S2, and Figure S2 (see footnote 1). Domain-wise probability density plots computed using spot dates with $<10\%$ uncertainty (2σ) relative to the absolute age are in Figures 14 and 15. For monazite dating, the monazite grains were mapped for Th, Y, U, and Pb to ensure that the spot (typically $<5 \mu\text{m}$ in diameter; larger at higher Th contents, $>10 \text{ wt}\% \text{ ThO}_2$) did not extend across boundaries between chemical domains identified based on Th and Y abundances (weak zoning in Pb and U zones were not helpful to distinguish chemical domains); this eliminates the possibility of mixing of different age domains, if any. Weight percent oxides total lying outside 98 and 102 wt% were excluded. Analyzed spot dates with 2σ error $>10\%$ (error percent computed following Prabhakar, 2013) were excluded. The monazite chemical dates reveal four major peak ages of 1710 ± 34 Ma (primarily from the Ranibandh granite), 1534 ± 35 Ma, 1305 ± 16 Ma, and 961 ± 9 Ma from the southern domain; the northern domain is characterized by a single peak age at 947 ± 11 Ma (Fig. 14; Table 2).

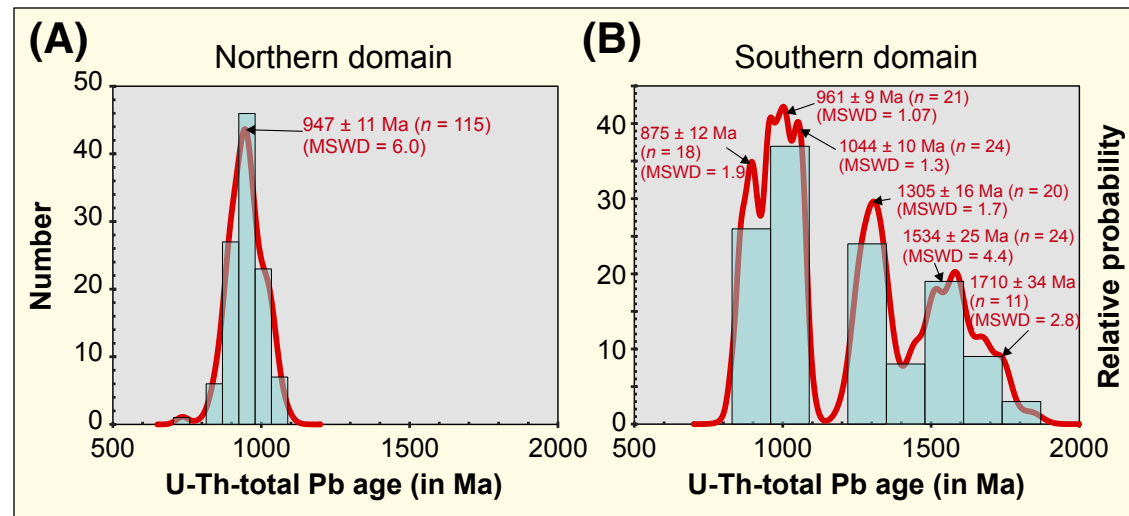


Figure 14. Probability-density plots monazite spot dates (this study) combined separately for the northern domain (A) and the southern domain (B). MSWD—mean square weighted deviation.

5.3 Synthesis of Ages of Geological Events across the Northern and Southern Domains

Monazites are especially susceptible to deformation-driven fluid-assisted alterations (Rasmussen et al., 2005). These alterations occur over a wide range of temperature (Poitrasson et al., 1996), much below the blocking temperature of lattice diffusion of Pb in monazite and zircon (Cherniak and Watson, 2001; Gardés et al., 2006). Therefore, monazites are ideally suited for recording low-temperature events (Rasmussen et al., 2005). These alterations modify the rare earth element abundances and U, Th, and Pb (and Y) contents in monazite, and this, in turn, leads to the modification of older ages in response to younger events (Hetherington et al., 2010). On the other hand, diffusive Pb loss in zircon is negligible at $T < 700$ °C (Cherniak and Watson, 2001).

5.3.1 Northern Domain

In the anatectic gneisses in the northern CGC domain, the metatexite layering is typically a pre- S_{1b} feature (Fig. 4A). Syn- D_{1b} leucosomes occurring as diatexite pods at D_{1b} boudin necks (Sequeira et al., 2020) are rare. In the CGC, available U-Pb zircon dates and chemical dates in metamorphic monazites suggest that this high-temperature anatectic event in quartzofeldspathic gneisses occurred between 1683 Ma and 1530 Ma (Acharyya, 2003; Rekha et al., 2011; Mukherjee et al., 2018a, 2018b; Sequeira and Bhattacharya, 2021; Sequeira et al., 2020, 2022).

Viewed in this perspective, the upper intercept age of 1762 ± 31 Ma retrieved from the anatectic gneiss WN-138A (Figs. 12 and 13) likely corresponds with pre- D_{1b} leucosome formation (metatexite layering) in the gneisses. The younger intercept date (1569 ± 13 Ma) in the zircon rims in the sample is inferred to be a metamorphic age identical with the concordant date 1569 ± 6 Ma obtained from the ESE-striking foliated granitoid (WN-4A; Fig. 13A), interpreted to be the emplacement age. The steeply dipping NNE-striking foliated pre- D_{1b} granitoid WN-63 yields two sets of concordant dates, 1670 ± 9 Ma and 1601 ± 4 Ma. Because the granitoid did not experience high-temperature (>550 °C) deformation-metamorphism post-dating its emplacement, the younger date (1601 ± 4 Ma) obtained in the oscillatory rims is taken to be the age of emplacement of the granitoid. The older concordant date (1670 ± 9 Ma) in the rock is likely inherited from the protolith from which the granitoid was derived. The date (1020 ± 4 Ma) of the ESE-striking foliated granitoid WN-43 is the youngest U-Pb (zircon) age recorded in this study from the CGC domain and is interpreted as an emplacement age. The granitoid possesses shallowly dipping mylonite fabric (D_2 deformation), and therefore the D_2 shortening deformation was younger than the age of emplacement of the granitoid WN-43.

In contrast to the large variations in the U-Pb zircon dates in the anatectic gneisses and granitoids in the northern domain, the chemical dates in metamorphic monazites lodged mostly within biotite-muscovite aggregates in the gneisses (sample WN-22a: 962 ± 13 Ma; WN-26A: 1012 ± 19 Ma and 924 ± 52 Ma; WN-140: 1028 ± 110 Ma and 904 ± 26 Ma) and in the mica schists (sample YD-7A: 916 ± 14 Ma; YD-7B: 1011 ± 23 Ma and 911 ± 16 Ma) lie between

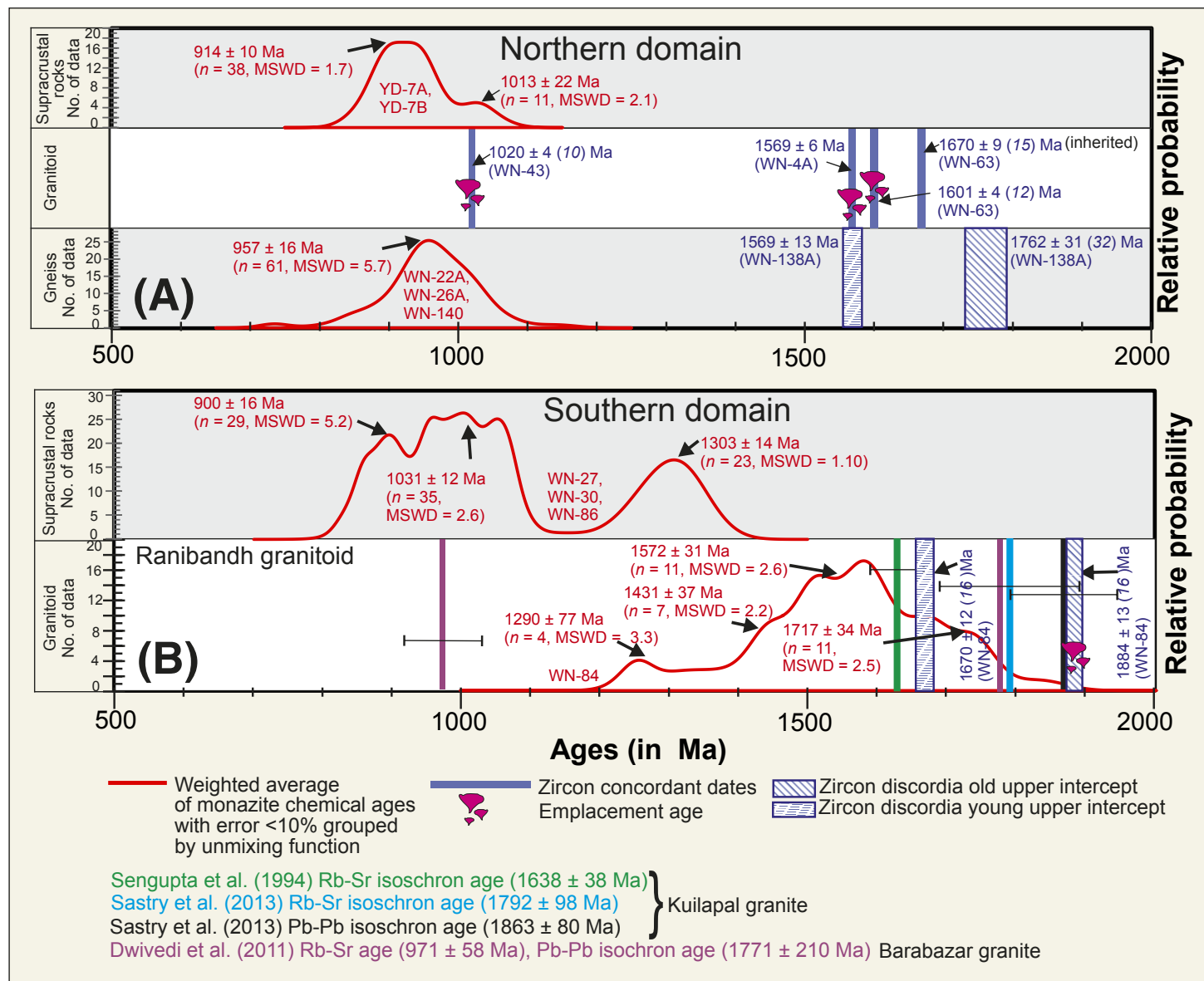


Figure 15. Zircon and monazite dates for northern domain (A) and southern domain (B). Ranibandh granitoid data are compared with available dates from Kuilapal and Barabazar granitoid plutons (data references are in figure). The error bar for the 975 Ma data is the 2σ error quoted by the original author. Vertical boxes are laser ablation inductively coupled plasma mass spectrometry U-Pb concordant and upper intercept discordia dates for zircon (box width is equivalent to 2σ errors). In the legend, “old upper intercept” and “young upper intercept” refer to the data shown in U-Pb concordia plots for southern domain Ranibandh granitoid WN-84 in Figure 13. For monazites, probability density curves are shown for chemical dates (weighted mean peak dates calculated using the unmix function of Isoplot software for spot dates with <10% error). MSWD—mean square weighted deviation.

1013 Ma and 914 Ma (Table 2; Text S2, Table S2, and Fig. S2 [see footnote 1]). This implies extensive early Neoproterozoic re-setting of older monazite dates in the CGC.

5.3.2 Southern Domain

In this study, we report for the first time LA-ICP-MS U-Pb (zircon) dates for the hitherto un-dated Ranibandh granitoid. We infer that the upper intercept date (1884 ± 13 Ma) of the older discordia for sample WN-84 represents the age of emplacement of the granitoid. The upper intercept date (1670 ± 12 Ma) of the younger discordia is likely a metamorphic age. Monazites in the same sample (WN-84) from the Ranibandh granitoid yield four statistically resolved mean population dates: 1717 ± 34 Ma, 1572 ± 31 Ma, 1431 ± 37 Ma, and 1290 ± 77 Ma; the oldest date is comparable with the U-Pb zircon metamorphic age of 1670 ± 12 Ma (Fig. 15B; Table 2).

By comparison, the chemical dates of metamorphic monazites in the schists in the southern domain (Figs. 14B and 15B; Table 2) are younger: sample WN-27 produced dates of 1045 ± 12 Ma, 956 ± 15 Ma, and 874 ± 15 Ma; WN-30, 1023 ± 23 Ma, 953 ± 12 Ma, and 873 ± 23 Ma; and WN-86, 1303 ± 14 Ma. Taken together, the mean population age peaks in metamorphic monazite in the schist and the Ranibandh granitoid (WN-84) are ca. 1720 Ma, ca. 1570–1290 Ma, and ca. 1020–900 Ma (Figs. 14B and 15). The monazite chemical ages at 1570 Ma and 1290 Ma in the southern domain are comparable with similar metamorphic ages recorded in the S-NSMB, south of the Dalma Belt (Mahato et al., 2008; Fig. 2B). Importantly, the 1020–910 Ma age range (Fig. 15B) coincides with the metamorphic monazite growth event in the northern domain at 1013–914 Ma (Fig. 15A).

6. DISCUSSION

6.1 Existence of Disparately Evolved Crustal Blocks within the SPSZ

The geologic events (metamorphism-deformation and felsic plutonism) in the northern CGC domain and the southern NSMB domain are summarized in Figure 16A. In the northern CGC domain, the pre- D_{1b} anatexis in the high-grade quartzofeldspathic gneiss (WN-138A) occurred at 1762 ± 31 Ma. This is consistent with the age of high-grade metamorphism-anatexis (D_{1a} - D_{1b}) at 1680–1530 Ma in the CGC (Acharyya, 2003; Sequeira and Bhattacharya, 2021; Sequeira et al., 2020, 2022), in the central and southern domains of the Satpura Mobile Belt (Bhandari et al., 2011), and in the Godhra–Chhota Udepur sector (Banerjee et al., 2021, 2022a, 2022b, 2022c). These anatectic gneisses in the northern domain were intruded by granitoids at 1569 ± 6 Ma (WN-4A), 1601 ± 4 Ma (WN-63), and 1020 ± 4 Ma (WN-43) (Table 2; Fig. 13). The youngest emplacement age of granitoid coincides with the age (1020–910 Ma) of metamorphic monazite in quartzofeldspathic gneisses and mica schist in the

northern domain (Fig. 15). But the mid-Mesoproterozoic events in the northern domain are not registered by monazites.

In the southern domain, the greenschist facies phyllites and schists record both mid-Mesoproterozoic (ca. 1303 Ma; Fig. 14) and early Neoproterozoic (1020–900 Ma; Figs. 14 and 15) ages. The monazites in the Ranibandh granitoid, however, record older metamorphic overprints at 1572–1431 Ma (Table 2) but share the younger metamorphic age at 1290 ± 77 Ma (Fig. 15) recorded in the greenschist facies mica schists and phyllites.

The emplacement age (1884 ± 13 Ma) of the Ranibandh granitoid in the southern domain is comparable to the SHRIMP U-Pb zircon date of 1861 ± 6 Ma determined for the Arkasani granophyre in the S-NSMB by Bhattacharya et al. (2015). These ages are older than the 1762–1612 Ma pre- D_{1b} high-temperature anatexis and metamorphism experienced by the quartzofeldspathic gneisses in the northern domain. Yet the 1884 ± 13 Ma Ranibandh granitoid did not experience the younger high-grade metamorphism-anatexis in the CGC gneisses. Also, in the S-NSMB block, there is, as yet, no evidence of mid-Mesoproterozoic and early Neoproterozoic felsic plutonism identified in the northern CGC domain and elsewhere in the CGC (Bhattacharya et al., 2023, and references therein). We infer, therefore, that the S-NSMB domain comprising the 1884 Ma Ranibandh pluton and the early to late Mesoproterozoic greenschist facies phyllites and schists evolved differently from the younger northern CGC block characterized by pre- D_{1b} early Mesoproterozoic high-grade metamorphism. Based on the disparate crustal evolutionary histories in the two domains and their shared metamorphic-structural and geochronological histories at 1020–910 Ma, it appears inescapable that the southern and the northern blocks were juxtaposed in the late Mesoproterozoic to early Neoproterozoic.

6.2 Nature of the 1.02–0.91 Ga Collision between the CGC and the NSMB along the SPSZ

At the northern margin of the NSMB, along the SPSZ (Fig. 3), both the D_2 deformation (top-to-the-south thrusting) and the D_3 deformation (nucleation of E-striking steeply dipping transpressional shearing) are shared by the NSMB and the CGC (Fig. 16B). The thrusting led to crustal thickening manifested by prograde loading (Fig. 11C) retrieved from the garnet-staurolite-bearing mica schist (sample WN-47A). This implies a southward translation of the CGC domain over the NSMB (Fig. 16B). Retardation in the rate of descent of the down-going NSMB slab followed by slab break-off caused the overlying lithosphere (the Dalma Belt) to extrude synchronously with continued N-S shortening (Fig. 16B). In the Gangpur schist belt, ~350 km to the west (Fig. 1C), Bhattacharya et al. (2019) suggested a subduction polarity reversal during 1.03–0.90 Ga collision between the Gangpur schist belt and the CGC; but the collision culminated with the CGC being the over-riding plate thrust southwards.

In response to the continued oblique D_2 and D_3 crustal shortening, the thickened crust accommodated the bulk strain by the nucleation of a network of steeply dipping transpressional shear zones that constitute the SPSZ

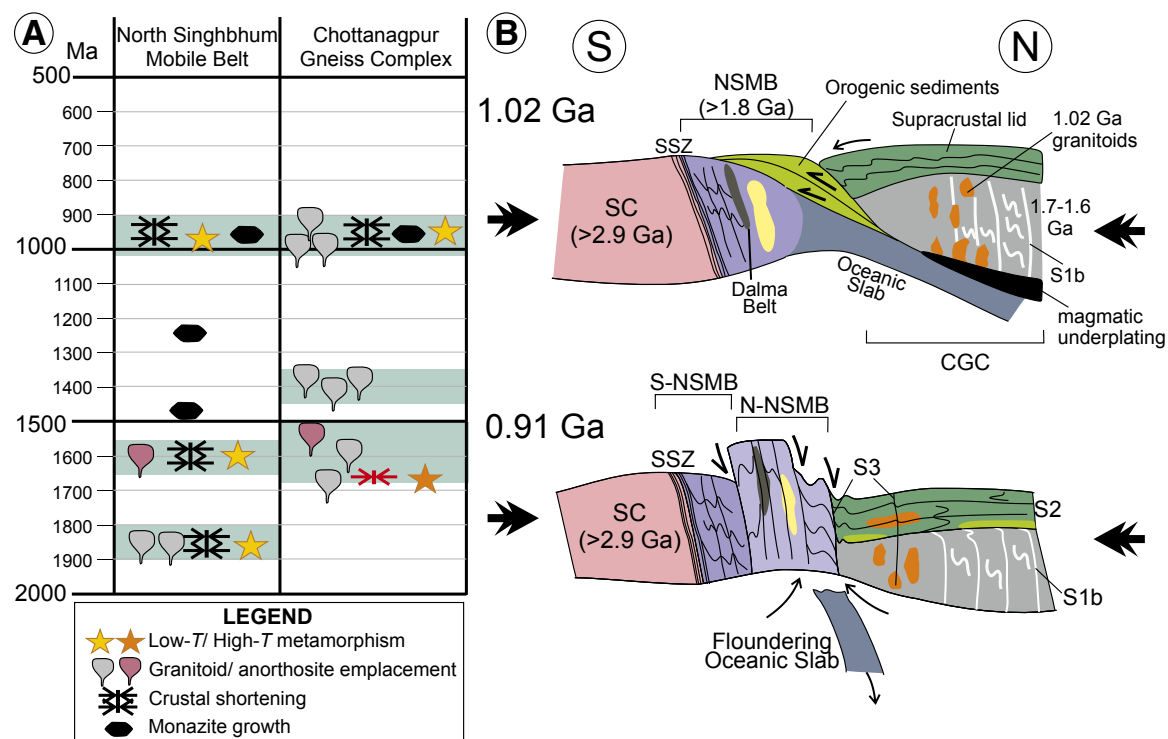


Figure 16. (A) Diagram showing differences in tectonic histories in Chottanagpur Gneiss Complex (CGC) and North Singhbhum Mobile Belt (NSMB) crustal domains, based on age data obtained from both domains (see text) and not restricted to this study only. Green horizontal bars represent duration of major phases of deformation-metamorphism and magmatic activities. *T*—temperature. **(B)** Tectonic cartoon showing two stages of NSMB-CGC collision between 1.02 Ga and 0.91 Ga along South Purulia Shear Zone (see text for details). Note that Rodinia-aged within-plate A-type granites occur exclusively within CGC and not within NSMB at the southern margin of Central Indian Tectonic Zone. This necessitates a northward Rodinia-age subduction followed by mantle delamination broadly synchronous with North India block–South India block collision. Large black arrows represent convergent directions. SC—Singhbhum Craton; N-NSMB—Northern NSMB; S-NSMB—Southern NSMB; CGC—Chottanagpur Gneiss Complex; SSZ—Singhbhum Shear Zone.

(Fig. 7). The bulk shortening strain largely accommodated by the rheologically weak micaceous rocks post-date the 1020 ± 4 Ma emplacement of the WN-43 granitoid. We interpret that the 1020–910 Ma chemical ages of metamorphic monazites aligned parallel to and overgrowing the S_2 and S_3 fabrics in both domains across the SPSZ correspond to the age of crustal shortening. The age coincides with the whole-rock Rb-Sr isochron age 971 ± 58 Ma of isotopic re-homogenization (Dwivedi et al., 2011).

A scrutiny of the four monazite-dated samples in the NSMB reveals that the mica schists WN-27 and WN-30 occur within the steeply dipping D_3 high-strain zone, but the mica schist WN-86 and the Ranibandh granitoid WN-84 are more centrally located within the SPSZ (Fig. 2A). The metamorphic monazites in mica

schists WN-27 and WN-30 are dated to be 1020–910 Ma, but the monazites in the mica schist WN-86 register ca. 1.30 Ga dates, and monazites in the Ranibandh granitoid (WN-84) record older dates, ca. 1720–1290 Ma. The last two samples do not record the early Neoproterozoic dates obtained from WN-27 and WN-30. It thus appears that monazites in the rocks closer to the Dalma Belt (Fig. 2) are unaffected by the D_3 deformation at 1020–910 Ma.

In summary, we suggest that the NSMB along its northern margin collided with the CGC in the early Neoproterozoic (1020–910 Ma). This is consistent with the results of earlier studies in different parts of the CITZ that suggest the assembly of the North India and South India blocks along the CITZ occurred between 1020 and 910 Ma, e.g., in the CGC (Bhattacharya et al., 2019; Sequeira

and Bhattacharya, 2021; Sequeira et al., 2020, 2022), the Satpura Mobile Belt (Chattopadhyay et al., 2020), and the Godhra–Chhota Udepur sector (Banerjee et al., 2021, 2022a, 2022b, 2022c).

6.3 NSMB: A Distinct Crustal Domain within the CITZ

The NSMB (Fig. 16A) is flanked by the Archean Singhbhum Craton (Olierook et al., 2019) in the south along the Singhbhum Shear Zone and the CGC along the SPSZ in the north (Fig. 2B). Mahato et al. (2008) constructed a 1520–1280 Ma amphibolite facies counter-clockwise *P-T* path for paraschists in the NSMB, south of the Dalma Belt (S-NSMB) (Fig. 2B). The authors correlated the *P-T* path with the collision of the Archean Singhbhum Craton and the S-NSMB. This collision age is comparable with a uraninite Pb-Pb age of 1580–1480 Ma obtained by Rao et al. (1979) for the Singhbhum Shear Zone (Figs. 1B and 1C). Johnson et al. (1993) obtained an older Pb-Pb age (1766 ± 82 Ma) for uraninite and sulfide mineralization for the Singhbhum Shear Zone.

Rekha et al. (2011) suggested that the 1520–1290 Ma metamorphism (Mahato et al., 2008) in the paraschists in the S-NSMB is lacking in the paraschists in the N-NSMB (Fig. 2B). The authors suggested the metamorphism in the schists and phyllites in the N-NSMB was early Neoproterozoic (ca. 950 Ma), consistent with this study (1020–910 Ma). In this study, 40 spots in metamorphic monazites in the muscovite schist (WN-86) and the Ranibandh granitoid (WN-84) yield dates between 1510 Ma and 1280 Ma. This indicates that the mid-Mesoproterozoic metamorphism related to the collision between the Archean Singhbhum Craton and the S-NSMB is indeed recorded in the N-NSMB (Fig. 2B). This contradicts the suggestion by Rekha et al. (2011) that the Dalma Belt acted as a “shield” that prevented the deformation-thermal effects of the Singhbhum Craton–NSMB collision from propagating into the N-NSMB.

We suggest therefore that the NSMB (Figs. 1B and 1C) that hosts the Dalma Belt is a distinct crustal domain with a hitherto unknown basement >1.9 Ga into which the Ranibandh granitoid intruded. Along its southern margin, the NSMB accreted with the Archean Singhbhum Craton at ca. 1.6–1.5 Ga. In the north, the NSMB was juxtaposed with the CGC along the SPSZ at 1.02–0.91 Ga (Fig. 16).

7. CONCLUDING REMARKS

The CITZ wedged between the North India and South India blocks (Fig. 1B) is an E-striking highly tectonized zone dominated overwhelmingly by Proterozoic rocks. In this study, we emphasize for the first time that the CITZ comprises multiple elongate crustal domains having distinctly different evolutionary histories, e.g., NSMB and CGC. These domains are intricately interleaved within the SPSZ along which the two crustal domains collided at 1.02–0.91 Ga. The oblique collision involved top-to-the-south thrusting of the CGC followed by nucleation of the left-lateral transpressional SPSZ prominently developed in the rheologically weak NSMB phyllites and schists. A consequence of this

finding is that the paleopole data in the North India and South India blocks that pre-date the collision event along the CITZ can be used only to determine the paleogeographic positions of the South India block or North India block separately and not of the Indian landmass, for the landmass did not come into existence before the early Neoproterozoic.

ACKNOWLEDGMENTS

Banerjee thanks the Department of Earth Sciences, Indian Institute of Technology (IIT) Bombay, for providing financial assistance through a post-doctoral research fellowship at IIT Bombay (HR-1[HRM 1]/Rect/34/2022). Naraga acknowledges the financial support (CRG/2019/000812) by the Scientific and Engineering Research Board for maintenance of the EPMA National Facility (Intensification of Research in High Priority Areas grant IR/S4/ESF-16/2009), Department of Earth Sciences, IIT Bombay. Himanshu S. Bai assisted with whole-rock analyses at the Sophisticated Analytical and Instrumentation Facility, IIT Bombay. We greatly appreciate the thoughtful, precise, and detailed comments of Lei Wu and two anonymous journal reviewers; their comments helped us to substantially improve the contents and styling of the manuscript. We greatly appreciate the editorial handling of the manuscript by Jiyuan Yin (Associate Editor) and Christopher Spencer (Science Editor).

REFERENCES CITED

- Acharjee, S., et al., 2016, Mineral chemistry of tourmaline from Mashak Pahar, South Purulia Shear Zone (SPSZ), eastern Indian Shield: *Journal of Earth System Science*, v. 125, p. 1681–1696, <https://doi.org/10.1007/s12040-016-0752-4>.
- Acharyya, A., Ray, S., Chaudhuri, B.K., Basu, S.K., Bhaduri, S.K., and Sanyal, A.K., 2006, Proterozoic rock suites along South Purulia Shear Zone, eastern India: Evidence for rift-related setting: *Journal of the Geological Society of India*, v. 68, p. 1069–1086.
- Acharyya, S.K., 2001, Geodynamic setting of the Central Indian Tectonic Zone in central, eastern and northeastern India: *Geological Survey of India Special Publications*, v. 64, p. 17–35.
- Acharyya, S.K., 2003, A plate tectonic model for Proterozoic crustal evolution of Central Indian Tectonic Zone: *Gondwana Geological Magazine*, v. 7, p. 9–31.
- Acharyya, S.K., and Roy, A., 2000, Tectonothermal history of the Central Indian Tectonic Zone and reactivation of major faults/shear zones: *Journal of the Geological Society of India*, v. 55, p. 239–256.
- Banerjee, A., Sequeira, N., and Bhattacharya, A., 2021, Tectonics of the Greater India Proterozoic Fold Belt, with emphasis on the nature of curvature of the belt in west-central India: *Earth-Science Reviews*, v. 221, <https://doi.org/10.1016/j.earscirev.2021.103758>.
- Banerjee, A., Sequeira, N., Cogné, N., Prabhakar, N., and Bhattacharya, A., 2022a, Early Neoproterozoic tectonics in the Godhra–Chhota Udepur sector: Evidence for two-stage accretion in the Great Indian Proterozoic Fold Belt: *Lithosphere*, v. 2022, <https://doi.org/10.2113/2022/9322892>.
- Banerjee, A., Cogné, N., Sequeira, N., and Bhattacharya, A., 2022b, Dynamics of Early Neoproterozoic accretion, west-central India: I. Geochronology and Geochemistry: *Lithos*, v. 422–423, <https://doi.org/10.1016/j.lithos.2022.106715>.
- Banerjee, A., Prabhakar, N., Sequeira, N., Cogné, N., and Bhattacharya, A., 2022c, Dynamics of Early Neoproterozoic accretion, west-central India: II –1.65 Ga HT-LP and –0.95 Ga LT-HP metamorphism in Godhra–Chhota Udepur, and a tectonic model for Early Neoproterozoic accretion: *Lithos*, v. 422–423, <https://doi.org/10.1016/j.lithos.2022.106740>.
- Basu, S.K., and Bhattacharyya, T., 2014, Petrography and mineral chemistry of Alkaline-Carbonatite Complex in Singhbhum Crustal Province, Purulia region, Eastern India: *Journal of the Geological Society of India*, v. 83, p. 54–70, <https://doi.org/10.1007/s12594-014-0007-4>.
- Bhandari, A., Pant, N.C., Bhowmik, S.K., and Goswami, S., 2011, ~1.6 Ga ultrahigh-temperature granulite metamorphism in the Central Indian Tectonic Zone: Insights from metamorphic reaction history, geothermobarometry and monazite chemical ages: *Geological Journal*, v. 46, p. 198–216, <https://doi.org/10.1002/gj.1221>.
- Bhattacharya, A., Mohanty, L., Maji, A., Sen, S.K., and Raith, M., 1992, Non-ideal mixing in the phlogopite-anne binary: Constraints from experimental data on Mg-Fe partitioning and a reformulation of the biotite-garnet geothermometer: *Contributions to Mineralogy and Petrology*, v. 111, p. 87–93, <https://doi.org/10.1007/BF00296580>.

- Bhattacharya, A., Rekha, S., Sequeira, N., and Chatterjee, A., 2019, Transition from shallow to steep foliation in the Early Neoproterozoic Gangpur accretionary orogen (Eastern India): Mechanics, significance of mid-crustal deformation, and case for subduction polarity reversal?: *Lithos*, v. 348–349, <https://doi.org/10.1016/j.lithos.2019.105196>.
- Bhattacharya, A., Banerjee, A., and Sequeira, N., 2023, The Central Indian Tectonic Zone: A Rodinia supercontinent-forming collision zone and analogy with the Grenville and Sveconorwegian orogens: *Geosphere*, v. 19, p. 1300–1317, <https://doi.org/10.1130/GES02597.1>.
- Bhattacharya, H.N., Nelson, D.R., Thern, E.R., and Altermann, W., 2015, Petrogenesis and geochronology of the Arkasani Granophyre and felsic Dalma volcanic rocks: Implications for the evolution of the Proterozoic North Singhbhum Mobile Belt, east India: *Geological Magazine*, v. 152, p. 492–503, <https://doi.org/10.1017/S0016756814000442>.
- Bhowmik, S.K., Wilde, S.A., Bhandari, A., Pal, T., and Pant, N.C., 2012, Growth of the Greater Indian Landmass and its assembly in Rodinia: Geochronological evidence from the Central Indian Tectonic Zone: *Gondwana Research*, v. 22, p. 54–72, <https://doi.org/10.1016/j.gr.2011.09.008>.
- Biswal, T.K., De Waele, D., and Ahuja, H., 2007, 2007, Timing and dynamics of the juxtaposition of the Eastern Ghats Mobile Belt against the Bhandara Craton, India: A structural and zircon U-Pb SHRIMP study of the fold-thrust belt and associated nepheline syenite plutons: *Tectonics*, v. 26, TC4006, <https://doi.org/10.1029/2006TC002005>.
- Chakrabarty, A., Mukherjee, S., Karmakar, S., Sanyal, S., and Sengupta, P., 2023, Petrogenesis and in situ U-Pb zircon dates of a suite of granitoid in the northern part of the Central Indian tectonic Zone: Implications for prolonged arc magmatism during the formation of the Columbia supercontinent: *Precambrian Research*, v. 387, <https://doi.org/10.1016/j.precamres.2023.106990>.
- Chatterjee, N., Mazumdar, A.C., Bhattacharya, A., and Saikia, R.R., 2007, Mesoproterozoic granulites of the Shillong-Meghalaya Plateau: Evidence of westward continuation of the Prydz Bay Pan-African suture into Northeastern India: *Precambrian Research*, v. 152, p. 1–26, <https://doi.org/10.1016/j.precamres.2006.08.011>.
- Chatterjee, N., Crowley, J.L., and Ghosh, N.C., 2008, Geochronology of the 1.55 Ga Bengal anorthosite and Grenvillian metamorphism in the Chotanagpur gneissic complex, eastern India: *Precambrian Research*, v. 161, p. 303–316, <https://doi.org/10.1016/j.precamres.2007.09.005>.
- Chatterjee, S.M., Sarkar, A.K., Roy, A., and Manna, A., 2020, Mid-Neoproterozoic tectonics of northwestern India: Evidence of stitching pluton along 810 Ma Phulad Shear Zone: *Tectonics*, v. 39, <https://doi.org/10.1029/2019TC005902>.
- Chattopadhyay, A., Bhowmik, S.K., and Roy, A., 2020, Tectonothermal evolution of the Central Indian Tectonic Zone and its implications for Proterozoic Supercontinent assembly: The current status: *Episodes: Journal of International Geosciences*, v. 43, p. 132–144, <https://doi.org/10.18814/epiugs/2020/020008>.
- Chaudhuri, T., Wan, Y., Mazumder, R., Ma, M., and Liu, D., 2018, Evidence of enriched, Hadean mantle reservoir from 4.2–4.0 Ga zircon xenocrysts from Paleoproterozoic TTGs of the Singhbhum Craton, Eastern India: *Scientific Reports*, v. 8, 7069, <https://doi.org/10.1038/s41598-018-25494-6>.
- Cherniak, D.J., and Watson, E.B., 2001, Pb diffusion in zircon: *Chemical Geology*, v. 172, p. 5–24, [https://doi.org/10.1016/S0009-2541\(00\)00233-3](https://doi.org/10.1016/S0009-2541(00)00233-3).
- Connolly, J.A.D., 2005, Computation of phase equilibria by linear programming: A tool for geodynamic modelling and its application to subduction zone decarbonation: *Earth and Planetary Science Letters*, v. 236, p. 524–541, <https://doi.org/10.1016/j.epsl.2005.04.033>.
- Deshmukh, T., Prabhakar, N., and Bhattacharya, A., 2021, Proterozoic high-temperature–low-pressure metamorphism in the Mahakoshal Belt, Central Indian Tectonic Zone (India): Structure, metamorphism, U-Th-Pb monazite geochronology, and tectonic implications: *The Journal of Geology*, v. 129, <https://doi.org/10.1086/715791>.
- Dewey, J.F., Holdsworth, R.E., and Strachan, R.A., 1998, Transpression and transtension zones, in Holdsworth, R.E., Strachan, R.A., and Dewey, J.F., eds., *Continental Transpressional and Transtensional Tectonics: Geological Society of London Special Publication 135*, p. 1–14, <https://doi.org/10.1144/GSL.SP.1998.135.01.01>.
- Dunkley, D.J., Clarke, G.L., and Harley, S.L., 1999, Diffusion metasomatism in silica-undersaturated sapphirine-bearing granulite from Rumdoodle Peak, Framnes Mountains, east Antarctica: *Contributions to Mineralogy and Petrology*, v. 134, p. 264–276, <https://doi.org/10.1007/s004100050483>.
- Dwivedi, A.K., Pandey, U.K., Murugan, C., Bhatt, A.K., Babu, P.V.R., and Joshi, M., 2011, Geochemistry and geochronology of A-type Barabazar granite: Implications on the geodynamics of South Purulia Shear Zone, Singhbhum craton, Eastern India: *Journal of the Geological Society of India*, v. 77, p. 527–538, <https://doi.org/10.1007/s12594-011-0055-y>.
- Ferry, J.M., and Spear, F.S., 1978, Experimental calibration of the partitioning of Fe and Mg between biotite and garnet: *Contributions to Mineralogy and Petrology*, v. 66, p. 113–117, <https://doi.org/10.1007/BF00372150>.
- Fossen, H., and Tikoff, B., 1998, Extended models of transpression and transtension, and application to tectonic settings, in Holdsworth, R.E., Strachan, R.A., and Dewey, J.F., eds., *Continental Transpressional and Transtensional Tectonics: Geological Society of London Special Publication 135*, p. 15–33, <https://doi.org/10.1144/GSL.SP.1998.135.01.02>.
- Gardés, E., Jaoul, O., Montel, J.-M., Seydoux-Guillaume, A.-M., and Wirth, R., 2006, Pb diffusion in monazite: An experimental study of Pb²⁺ + Th⁴⁺ ↔ 2Nd³⁺ interdiffusion: *Geochimica et Cosmochimica Acta*, v. 70, p. 2325–2336, <https://doi.org/10.1016/j.gca.2006.01.018>.
- Ghosh, S.K., 1959a, Migmatization in relation to regional deformation in the area around Kailapal, W. Bengal: *Quarterly Journal of the Geological, Mining, and Metallurgical Society of India*, v. 31, p. 171–176.
- Ghosh, S.K., 1959b, Crystallisation in relation to periods of deformation in the pelitic schists around the Kailapal granite-gneiss in S.W. West Bengal, in *Indian Science Congress Association Proceedings of the Forty-Sixth Session, Part III: Abstracts: Calcutta, Indian Science Congress Association*, p. 215.
- Ghosh, S.K., Sen, G., and Sengupta, S., 2003, Rotation of long tectonic clasts in transpressional shear zones: *Journal of Structural Geology*, v. 25, p. 1083–1096, [https://doi.org/10.1016/S0191-8141\(02\)00146-3](https://doi.org/10.1016/S0191-8141(02)00146-3).
- Geological Survey of India, 2001a, District Resource Map—Puruliya, West Bengal: Geological Survey of India, Kolkata, scale 1:250,000.
- Geological Survey of India, 2001b, District Resource Map—Bankura, West Bengal: Geological Survey of India, Kolkata, scale 1:250,000.
- Geological Survey of India, 2006, District Resource Map—East Singhbhum, Jharkhand: Geological Survey of India, Kolkata, scale 1:250,000.
- Hetherington, C.J., Harlov, D.E., and Budzyń, B., 2010, Experimental metasomatism of monazite and xenotime: Mineral stability, REE mobility and fluid composition: *Mineralogy and Petrology*, v. 99, p. 165–184, <https://doi.org/10.1007/s00710-010-0110-1>.
- Holdaway, M.J., 2000, Application of new experimental and garnet Margules data to the garnet-biotite geothermometer: *American Mineralogist*, v. 85, p. 881–892, <https://doi.org/10.2138/am-2000-0701>.
- Holdaway, M.J., Mukhopadhyay, B., Dyar, M.D., Guidotti, C.V., and Dutrow, B.L., 1997, Garnet-biotite geothermometry revised: New Margules parameters and a natural specimen data set from Maine: *American Mineralogist*, v. 82, p. 582–595, <https://doi.org/10.2138/am-1997-5-618>.
- Holland, T., and Powell, R., 2001, Calculation of phase relations involving haplogranitic melts using an internally consistent thermodynamic dataset: *Journal of Petrology*, v. 42, p. 673–683, <https://doi.org/10.1093/ptrology/42.4.673>.
- Horstwood, M.S.A., et al., 2016, Community-derived standards for LA-ICP-MS U-(Th)-Pb geochronology—Uncertainty propagation, age interpretation and data reporting: *Geostandards and Geoanalytical Research*, v. 40, p. 311–332, <https://doi.org/10.1111/j.1751-908X.2016.00379.x>.
- Johnson, P.T., Dasgupta, D., and Smith, A.D., 1993, Pb–Pb systematic of copper sulphide mineralization, Singhbhum area, Bihar: *Indian Journal of Geology*, v. 69, p. 211–213.
- Kaneko, Y., and Miyano, T., 2004, Recalibration of mutually consistent garnet–biotite and garnet–cordierite geothermometers: *Lithos*, v. 73, p. 255–269, <https://doi.org/10.1016/j.lithos.2003.12.009>.
- Kruhl, J.H., 1996, Prism- and basal-plane parallel subgrain boundaries in quartz: A microstructural geothermobarometer: *Journal of Metamorphic Geology*, v. 14, p. 581–589, <https://doi.org/10.1046/j.1525-1314.1996.00413.x>.
- Li, Z.X., et al., 2008, Assembly, configuration, and break-up history of Rodinia: A synthesis: *Precambrian Research*, v. 160, p. 179–210, <https://doi.org/10.1016/j.precamres.2007.04.021>.
- Ludwig, K.R., 2012, User's manual for Isoplot version 3.75–4.15: A geochronological toolkit for Microsoft Excel: *Berkeley Geochronological Center Special Publication 5*.
- Mahato, S., Goon, S., Bhattacharya, A., Mishra, B., and Bernhardt, H.-J., 2008, Thermo-tectonic evolution of the North Singhbhum Mobile Belt (eastern India): A view from the western part of the belt: *Precambrian Research*, v. 162, p. 102–127, <https://doi.org/10.1016/j.precamres.2007.07.015>.
- Maji, A.K., Goon, S., Bhattacharya, A., Mishra, B., Mahato, S., and Bernhardt, H.-J., 2008, Proterozoic polyphase metamorphism in the Chotanagpur Gneissic Complex (India), and implication for trans-continental Gondwanaland correlation: *Precambrian Research*, v. 162, p. 385–402, <https://doi.org/10.1016/j.precamres.2007.10.002>.

- Merdith, A.S., et al., 2021, Extending full-plate tectonic models into deep time: Linking the Neoproterozoic and the Phanerozoic: *Earth Science Reviews*, v. 214, <https://doi.org/10.1016/j.earscirev.2020.103477>.
- Mohanty, S.P., 2023, Paleoproterozoic thick-skinned tectonics in the Central Indian Tectonic Zone: Implications on the tectonic reconstructions of cratonic nuclei: *International Geology Review*, v. 65, p. 3028–3064, <https://doi.org/10.1080/00206814.2023.2172620>.
- Montel, J.-M., Foret, S., Veschambre, M., Nicollet, C., and Provost, A., 1996, Electron microprobe dating of monazite: *Chemical Geology*, v. 131, p. 37–53, [https://doi.org/10.1016/0009-2541\(96\)00024-1](https://doi.org/10.1016/0009-2541(96)00024-1).
- Mukherjee, S., Dey, A., Ibanez-Mejia, M., Sanyal, S., and Sengupta, P., 2018a, Geochemistry, U-Pb geochronology and Lu-Hf isotope systematics of a suite of ferroan (A-type) granitoids from the CGGC: Evidence for Mesoproterozoic crustal extension in the east Indian shield: *Precambrian Research*, v. 305, p. 40–63, <https://doi.org/10.1016/j.precamres.2017.11.018>.
- Mukherjee, S., Dey, A., Sanyal, S., and Sengupta, P., 2018b, Tectonothermal imprints in a suite of mafic dykes from the Chotanagpur Granite Gneissic complex (CGGC), Jharkhand, India: Evidence for late Tonian reworking of an early Tonian continental crust: *Lithos*, v. 320–321, p. 490–514, <https://doi.org/10.1016/j.lithos.2018.09.014>.
- Nasipuri, P., Bhattacharya, A., and Das, S., 2009, Metamorphic reactions in dry and aluminous granulites: A *Perple_X* *P-T* pseudosection analysis of the influence of effective reaction volume: Contributions to Mineralogy and Petrology, v. 157, p. 301–311, <https://doi.org/10.1007/s00410-008-0335-8>.
- Nasipuri, P., Corfu, A., and Bhattacharya, A., 2018, Eastern Ghats Province (India)–Rayner Complex (Antarctica) accretion: Timing the event: *Lithosphere*, v. 10, p. 523–529, <https://doi.org/10.1130/L703.1>.
- Newton, R., Wood, B., and Kleppa, O., 1981, Thermochemistry of silicate solid solutions: *Bulletin de Minéralogie*, v. 104, p. 162–171, <https://doi.org/10.3406/bulmi.1981.7451>.
- Olierook, H.K.H., Clark, C., Reddy, S.M., Mazumder, R., Jourdan, F., and Evans, N.J., 2019, Evolution of the Singhbhum Craton and supracrustal provinces from age, isotopic and chemical constraints: *Earth-Science Reviews*, v. 193, p. 237–259, <https://doi.org/10.1016/j.earscirev.2019.04.020>.
- Perchuk, L.L., 1989, *P-T*-fluid regimes of metamorphism and related magmatism with specific reference to the granulite-facies Sharyzhgaysk complex of Lake Baikal, in Daly, J.S., Cliff, R.A., and Yardley, B.W.D., eds., *Evolution of Metamorphic Belts: Geological Society of London Special Publication 43*, p. 275–291, <https://doi.org/10.1144/GSL.SP.1989.043.01.19>.
- Pisarevsky, S.A., Biswal, T.K., Wang, X.-C., De Waele, B.E., Ernst, R., Söderlund, U., Tait, J.A., Ratre, K., Singh, Y.K., and Cleve, M., 2013, Palaeomagnetic, geochronological, and geochemical study of Mesoproterozoic Lakhna Dykes in the Bastar Craton, India: Implications for the Mesoproterozoic supercontinent: *Lithos*, v. 174, p. 125–143, <https://doi.org/10.1016/j.lithos.2012.07.015>.
- Poitrasson, F., Chenery, S., and Bland, D.J., 1996, Contrasted monazite hydrothermal alteration mechanisms and their geochemical implications: *Earth and Planetary Science Letters*, v. 145, p. 79–96, [https://doi.org/10.1016/S0012-821X\(96\)00193-8](https://doi.org/10.1016/S0012-821X(96)00193-8).
- Powell, R., and Evans, J.A., 1983, A new geobarometer for the assemblage biotite-muscovite-chlorite-quartz: *Journal of Metamorphic Geology*, v. 1, p. 331–336, <https://doi.org/10.1111/j.1525-1314.1983.tb00278.x>.
- Prabhakar, N., 2013, Resolving poly-metamorphic Paleoproterozoic ages by chemical dating of monazites using multi-spectrometer U, Th and Pb analyses and sub-counting methodology: *Chemical Geology*, v. 347, p. 255–270, <https://doi.org/10.1016/j.chemgeo.2013.04.012>.
- Prabhakar, N., and Bhattacharya, A., 2013, Paleoproterozoic partial convective overturn in the Singhbhum Craton, Eastern India: *Precambrian Research*, v. 231, p. 106–121, <https://doi.org/10.1016/j.precamres.2013.03.009>.
- Praharaj, O., Rekha, S., and Bhattacharya, A., 2021, Structure and chronology across the Achanakovil terrain boundary shear zone system (South India), and its Madagascar connection in the Gondwanaland: *International Journal of Earth Sciences*, v. 110, p. 1545–1573, <https://doi.org/10.1007/s00531-021-02029-5>.
- Rao, N.K., Aggarwal, S.K., and Rao, G.V.U., 1979, Lead isotopic ratios of uraninites and the age of uranium mineralization in Singhbhum Shear Zone, Bihar: *Journal of the Geological Society of India*, v. 20, p. 124–127.
- Rasmussen, B., Fletcher, I.R., and Sheppard, S., 2005, Isotopic dating of the migration of a low-grade metamorphic front during orogenesis: *Geology*, v. 33, p. 773–776, <https://doi.org/10.1130/G21666.1>.
- Rekha, S., and Bhattacharya, A., 2014, Paleoproterozoic/Mesoproterozoic tectonism in the northern fringe of the Western Dharwar Craton (India): Its relevance to Gondwanaland and Columbia supercontinent reconstructions: *Tectonics*, v. 33, p. 552–580, <https://doi.org/10.1002/2013TC003335>.
- Rekha, S., Upadhyay, D., Bhattacharya, A., Kooijman, E., Goon, S., Mahato, S., and Pant, N.C., 2011, Lithostructural and chronological constraints for tectonic restoration of Proterozoic accretion in the Eastern Indian Precambrian shield: *Precambrian Research*, v. 187, p. 313–333, <https://doi.org/10.1016/j.precamres.2011.03.015>.
- Ring, U., and Glodny, J., 2010, No need for lithospheric extension for exhuming (U)HP rocks by normal faulting: *Journal of the Geological Society*, v. 167, p. 225–228, <https://doi.org/10.1144/0016-76492009-134>.
- Rivers, T., 2015, Tectonic setting and evolution of the Grenville Orogen: An assessment of progress over the last 40 years: *Geoscience Canada*, v. 42, p. 77–124, <https://doi.org/10.12789/geocanj.2014.41.057>.
- Roy, A., Sarkar, A., Jeyakumar, S., Aggrawal, S.K., and Ebihara, M., 2002, Mid-Proterozoic plume-related thermal event in eastern Indian craton: Evidence from trace elements, REE geochemistry and Sr-Nd isotope systematics of basic-ultrabasic intrusive from Dalma volcanic belt: *Gondwana Research*, v. 5, p. 133–146, [https://doi.org/10.1016/S1342-937X\(05\)70897-2](https://doi.org/10.1016/S1342-937X(05)70897-2).
- Sarkar, S.N., Ghosh, D.K., and St Lambert, R.J., 1986, Rubidium-strontium and lead isotopic studies of the soda-granites from Musaboni area, Singhbhum Copper Belt, E. India, in Sarkar, S.N., ed., *Geology and Geochemistry of Sulphide Ore Bodies and Associated Rocks in Musaboni and Rakha Mines Sections in the Singhbhum Copper Belt: Dhanbad, Indian School of Mines, Diamond Jubilee Monograph*, p. 101–110.
- Sastry, D.V.L.N., Pandey, U.K., and Pandey, B.K., 2013, Rb-Sr and Pb-Pb geochronological studies on the granite gneisses of Kulupal, Purulia-Bankura Midnapore districts, West Bengal: *Journal of Applied Geochemistry*, v. 15, p. 19–24.
- Schlunegger, F., and Kissling, E., 2015, Slab rollback orogeny in the Alps and evolution of the Swiss Molasse basin: *Nature Communications*, v. 6, 8605, <https://doi.org/10.1038/ncomms9605>.
- Sengupta, S., Paul, D.K., Bishui, P.K., Gupta, S.N., Chakraborty, R., and Sen, P., 1994, A geochemical and Rb-Sr isotopic study of Kulupal granite and Arkasoni granophyre from the eastern Indian craton: *Indian Minerals*, v. 48, p. 77–88.
- Sequeira, N., and Bhattacharya, A., 2020, Early Neoproterozoic deformation kinematics in the Chottanagpur Gneiss Complex (eastern India): Evidence from the curvilinear Hundru Falls Shear Zone Analysis: *Lithosphere*, v. 2020, <https://doi.org/10.2113/2020/8820919>.
- Sequeira, N., and Bhattacharya, A., 2021, Early Neoproterozoic accretion at the northern margin of the Chottanagpur Gneiss Complex, Eastern India: *Tectonics*, v. 40, <https://doi.org/10.1029/2020TC006613>.
- Sequeira, N., Mahato, S., Rahl, J.M., Sarkar, S., and Bhattacharya, A., 2020, The anatomy and origin of a synconvergent Grenvillian-age metamorphic core complex, Chottanagpur Gneiss Complex, eastern India: *Lithosphere*, v. 2020, <https://doi.org/10.2113/2020/8833404>.
- Sequeira, N., Bhattacharya, A., and Bell, E., 2022, The ~1.4Ga A-type granitoids from the “Chottanagpur crustal block” (India), and its relocation from Columbia to Rodinia?: *Geoscience Frontiers*, v. 13, 101138, <https://doi.org/10.1016/j.gsf.2020.12.017>.
- Spencer, C.J., Hawkesworth, C., Cawood, P.A., and Dhuime, B., 2013, Not all supercontinents are created equal: Gondwana-Rodinia case study: *Geology*, v. 41, p. 795–798, <https://doi.org/10.1130/G34520.1>.
- Vigneresse, J.L., and Burg, J.P., 2000, Continuous vs. discontinuous melt segregation in migmatites: Insights from a cellular automation model: *Terra Nova*, v. 12, p. 188–192, <https://doi.org/10.1046/j.1365-3121.2000.00299.x>.
- Waldbaum, D.R., and Thompson, J.B., Jr., 1968, Mixing properties of sanidine crystalline solutions: II. Calculations based on volume data: *American Mineralogist*, v. 53, p. 2000–2017.
- White, R.W., Powell, R., and Holland, T.J.B., 2007, Progress relating to calculation of partial melting equilibria for metapelites: *Journal of Metamorphic Geology*, v. 25, p. 511–527, <https://doi.org/10.1111/j.1525-1314.2007.00711.x>.
- White, R.W., Powell, R., and Johnson, T.E., 2014, The effect of Mn on mineral stability in metapelites revisited: New *a-x* relations for manganese-bearing minerals: *Journal of Metamorphic Geology*, v. 32, p. 809–828, <https://doi.org/10.1111/jmg.12095>.
- Whitney, D.L., and Evans, B.W., 2010, Abbreviations for names of rock-forming minerals: *American Mineralogist*, v. 95, p. 185–187, <https://doi.org/10.2138/am.2010.3371>.
- Wu, C.-M., and Zhao, G., 2006, Recalibration of the garnet-muscovite (GM) geothermometer and the garnet-muscovite-plagioclase-quartz (GMPQ) geobarometer for metapelitic assemblages: *Journal of Petrology*, v. 47, p. 2357–2368, <https://doi.org/10.1093/petrology/egl047>.
- Yedekar, D.B., Jain, S.C., Nair, K.K.K., and Dutta, K.K., 1990, The Central Indian collision suture, in *Precambrian of Central India: Geological Survey of India Special Publication 28*, p. 1–43.